Chapter 5

Results for coronal holes, quiet sun and plumes

This Chapter presents a selection of 'typical' results from the analyses of coronal hole and quiet sun regions, and of coronal hole plumes, using the data described in Chapter 4. First, off-limb densities and temperatures derived from 1996 to 1998 quiet sun and coronal hole observations, are presented in Section 5.1, to show the main differences between these regions, and how they have not significantly changed over that period. Secondly, results from some of the near Sun centre observations done in 1996 are presented in Section 5.2. They include densities, temperatures and abundances for the Elephant's Trunk coronal hole, a nearby quiet sun region and a low-latitude plume. These observations are then compared and summarised in Section 5.2.4.

Part of the analyses done have already been published (see below for details), and the results are only outlined here. Some of the data presented in these published papers have been re-analysed for this thesis using the most up-to-date instrument calibration (Chapter 3), improved atomic physics, and different ionization equilibrium. The results of these re-analyses, presented here, do not affect the main findings, but have some differences from those already published. It is important to make clear which are the main reasons for these differences.

- A new instrument calibration (Chapter 3) has been adopted.

  While results based on lines close in wavelength and seen in the same detector (as the densities based on the Si IX and Si X line ratios, for example) are not much dependent on the calibration, others, such as those derived from the use of the Mg and Ne lines seen in NIS 1 and NIS 2, can be different by a factor of 2, depending on which calibration is adopted. Since the Mg/Ne abundance is the only one that can be used to constrain the relative abundances of all the other high- and low-FIP ions (if only NIS observations are used), a different calibration affects results in terms of

FIP effect. Also, with the calibration adopted here, many bright coronal lines (Mg X, Al XI, Si XII) seen in NIS 2 are not in good agreement with those observed in NIS 1, as already seen.

- A different ionization equilibrium. Here, the *Arnaud and Rothenflug* (1985) ionization equilibrium for all the ions has been adopted, together with the calculations of *Landini and Monsignori Fossi* (1991) for the minor elements. In some of the previous publications the *Arnaud and Raymond* (1992) calculations for Fe were used. Chapter 3 already illustrated some of the differences that are found when other ionization equilibrium calculations are adopted, with variations of a factor of almost 2 for some ions, and how the *Arnaud and Rothenflug* (1985) calculations give more consistent results between most of the ions. Different choices of ionization equilibrium affect both the *DEM* distribution (although slightly), and the relative element abundances that are found with the use of any differential emission measure (or line emission measure) method.

  The *Arnaud and Rothenflug* (1985) ionization equilibrium has been assumed here in deriving all isothermal temperatures from line ratios.

- More recent atomic data, in the form of CHIANTI v.2 (*Landi et al.*, 1999b) have been used. The main differences between CHIANTI v.2 and the previous versions, that concern the results presented here, are new calculations for Ne IV, Ne VII, and Fe X, together with the inclusion of many new ions. The differences in the emissivities are considerable for some lines. Then, CHIANTI v.2 contains a correction for an error in the earlier O IV database, that affected the 608.4 and 609 Å lines, such that densities derived using the 608.4 Å line were overestimated by about a factor of 2.

  In addition to the CHIANTI upgrade, recent Fe XIV calculations (*Storey et al.*, 1999) and Mg IX calculations (P. Young, 1999, priv. comm.) have been used here, although the differences for Mg IX are small and the Fe XIV lines are weak or absent from the spectra used. For those ions that are not present in the CHIANTI database, the Arcetri spectral code (AC, see, e.g. *Landi and Landini*, 1998a) was used. The continuum emission has been calculated with the method described in *Landi et al.* (1999b).

5.1 General characteristics of off-limb densities and temperatures for the quiet sun and polar coronal holes from 1996 to 1998

August 1996 was a good choice for the Whole Sun Month (WSM) international campaign. During this month, there was little variation in longitude of the equatorial streamer structure (in particular around the 20th), as shown for example by coronagraph images, and this simple structure became the best test the Sun could offer for comparisons of different instruments' data and modelling. Two workshops were organised to coordinate the effort, and the author actively participated in these. The main outcome of the WSM campaign has been a series of refereed journal papers, collected into a special issue of the Journal of Geophysical Research – Space Physics in May 1999. As well as leading one paper, the author contributed directly to two papers doing a large part of the data analysis and providing software (*Fludra et al.*, 1999a; *Gibson et al.*, 1999). Preliminary results were given by *Fludra et al.* (1997a), and *Fludra et al.* (1997b). The observations that were analysed in collaboration with A. Fludra, together with the main results, are presented in this Section.

Off-limb observations of the equatorial regions

From the large data set presented in Chapter 4, NIS data taken on six days were selected for analysis of the equatorial regions above the east/west limb. Three pairs of dates approximately half a solar rotation period apart were chosen: 12 and 27 August, 15 and 30 August, and 19 August and 3 September. This allowed direct comparison of the same location viewed both on the East and West limb to check the time variability in the coronal streamer structure. In addition, the dates of 12 and 19 August (and 27 August and 3 September) are seven days apart, thus sampling different areas separated by 90 degrees in longitude. All of the monochromatic images obtained for the above dates showed quiet Sun areas, almost free from any active region emission. In two cases where active region loops were present, these areas were excluded from analysis, and only the quiet part of the solar corona was analysed.

As an example, some results for the off-limb observation of on 1996 August 19 are presented here. The data have been averaged along concentric arcs of constant radius and spanning a range of position angles, to produce (after a multi-gaussian fit to the spectra) an averaged radial dependence of the line intensities. From these, physical parameters such as electron density and temperature have been derived as a function of the radial distance above the limb. Spatial averaging along concentric arcs increased the signal-to-noise, allowing

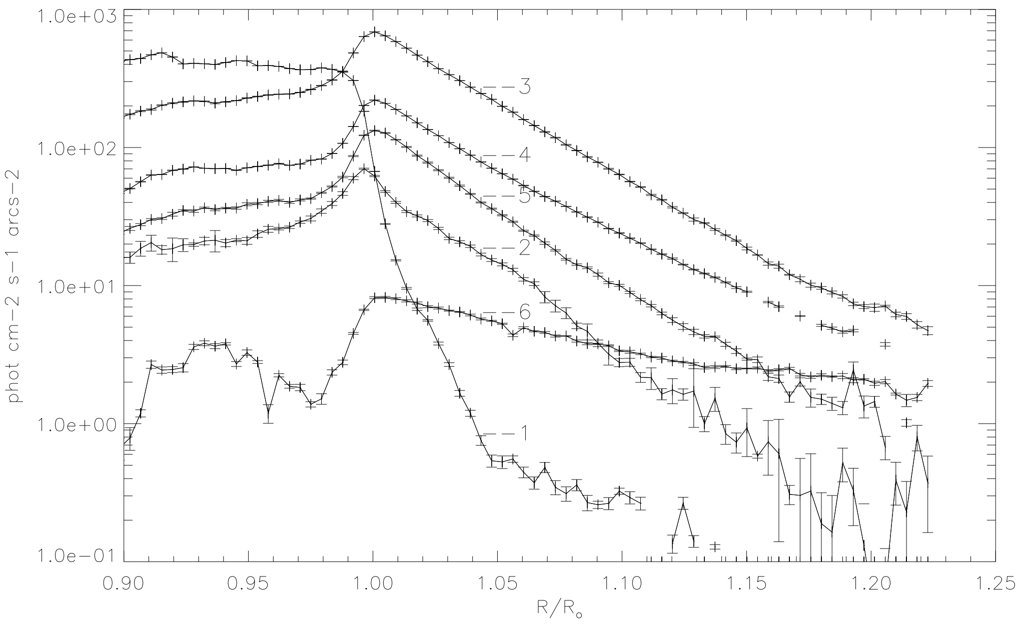

Figure 5.1: *The off-limb intensities of selected lines – 19th August 1996, plotted on a log scale. 1: He I 584.3 Å; 2: Mg VII 367.7 Å; 3: Mg IX 368.1 Å; 4: Mg X 624.9 Å; 5: Si IX 349.9 Å; 6: Si XII 520.7 Å. Note the different slopes of intensities versus radial distance above the limb.*

measurement of the coronal line intensities up to 1.2 $R_\odot$. These are shown in Figure 5.1. Note: (1) the rapid drop of the He I intensity, showing there is little off-limb stray light; (2) how the line intensities have near-exponential decreases, with different slopes for different lines.

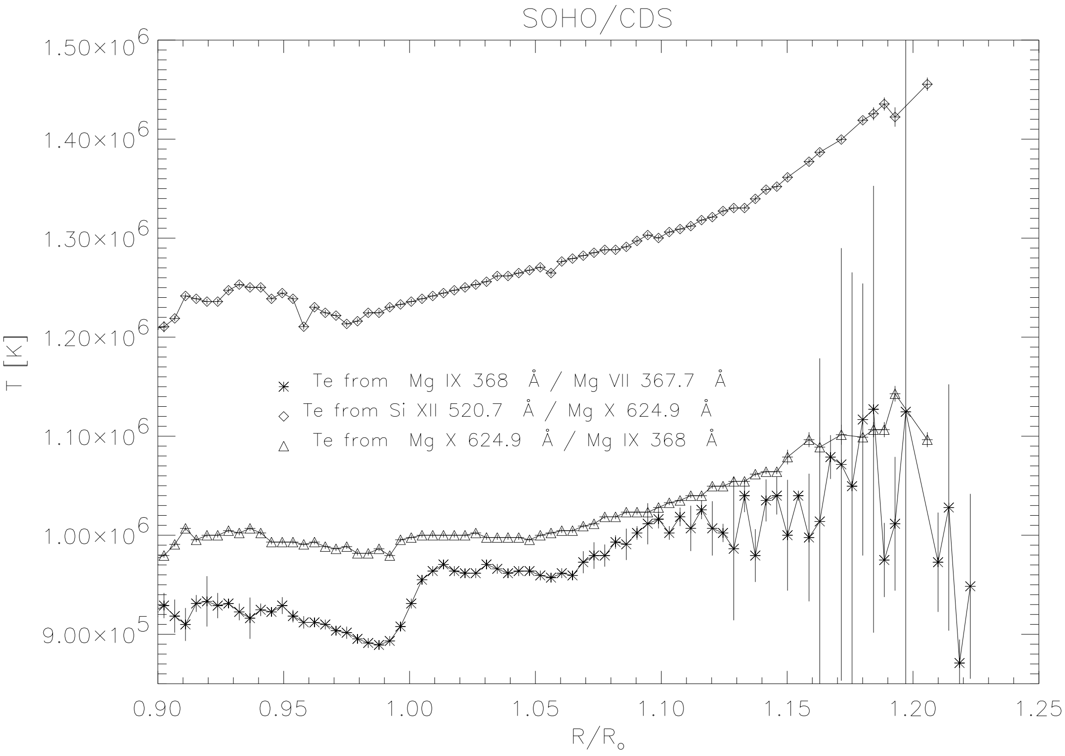

Figure 5.2: *The off-limb isothermal temperatures as derived from different line ratios. – 19th August 1996. The temperature from the Si XII / Mg X ratio was derived assuming photospheric abundances.*

Figure 5.2 shows the isothermal temperatures as derived from various line ratios. The fact that the various ratios yield different temperatures shows that the plasma was not strictly isothermal at those radial distances. Each temperature increases by about 10% from the limb to 1.2 $R_\odot$.

Figure 5.3 shows how the two Si IX lines used for density estimates, have different radial profiles, and how the derived density (that is an average along the line of sight) decreases from 5 x10^8 on the disc and at the limb, to 1 x10^8 (cm^{-3}) at 1.2 $R_\odot$.

Further results are presented in *Fludra et al.* (1999a) and *Gibson et al.* (1999). Electron densities were derived from the observed Si IX 349.9/341.9 Å ratio, while isothermal temperatures from Si XII/Mg X and Si XII/Mg IX ratios were calculated up to 0.2 $R_\odot$ above the limb. The results showed little time variability over a period of 20 days. Densities in the streamer region decreased exponentially with height, while temperatures showed an

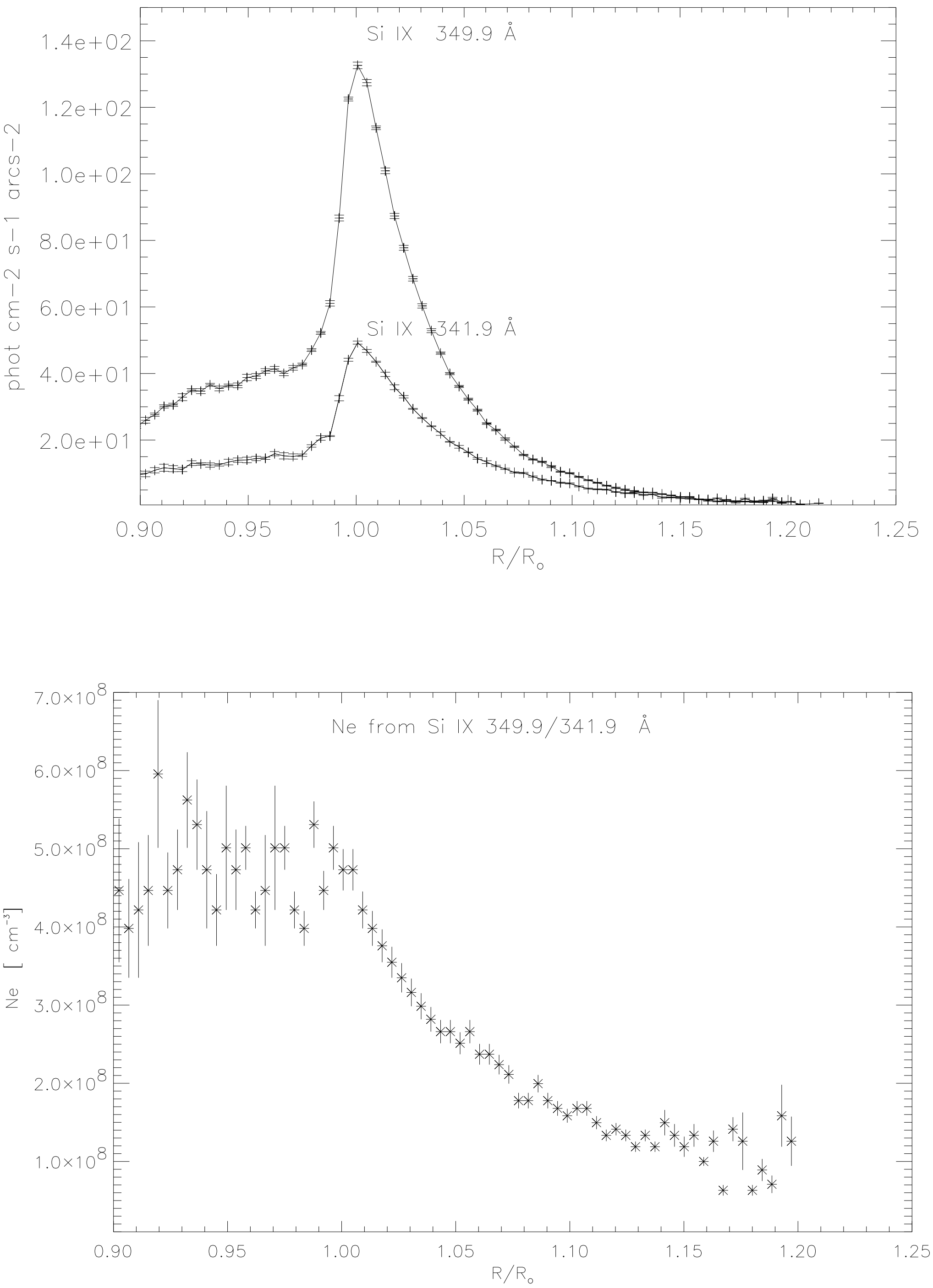

Figure 5.3: *The off-limb intensities of the two Si IX lines (above) and the derived densities (below) – 19th August 1996.*

increase up to 1.2 $R_\odot$ after which they maintained level values. A comparison with Yohkoh SXT data (*Fludra et al.* 1999a) showed a good agreement in terms of temperatures, for the streamer region of August 19. This direct comparison of nearly-simultaneous observations of a simple structure indicates that the results from direct EUV line intensities and broad-band filter ratio techniques can sometimes be in good agreement.

The streamer data were used by *Gibson et al.* (1999) for a comparison with results from white-light data. The densities determined from CDS and those determined from the *van de Hulst* (1950) inversion technique were very similar. This allowed the radial dependence of the electron density (averaged along the line of sight) over the 1–4 $R_\odot$ range to be simultaneously determined for the first time. Remembering that the white light intensity is proportional to an integral of N_e along the line of sight , while EUV line intensities depend on ${N_\mathrm{e}}^2$, this result is quite remarkable.

Polar coronal holes

The North polar coronal hole observations of 1996 August 24, 31, and September 7, and South polar coronal hole observations of August 18 were analysed for the *Fludra et al.* (1999a) paper. The same spatial averaging along concentric arcs of constant radius described above was applied to the data.

Some preliminary results were given by *Fludra et al.* (1997a) and *Fludra et al.* (1997b), while a more complete analysis is presented in *Fludra et al.* (1999a). Densities and temperatures of the polar coronal hole regions were obtained using the same diagnostics described above. The main results are that densities and temperatures were lower in coronal holes, and that the derived values presented little variability over that period. Densities were decreasing with height, having lower values (by about a factor of 2) compared to the equatorial regions.

A similar analysis of off-limb NIS spectra was repeated on further sets of coronal hole observations, planned and executed in 1997 and 1998 by A. Fludra. Some of the results obtained are described in *Fludra et al.* (1999b), and are not repeated here. One remarkable result is that densities and temperatures showed similar values to those of August 1996.

5.2 Results from near-disc-centre observations, 1996 August

Coronal hole CDS observations of the 1996 August 26 and 27, which benefited from a near-radial line of sight, are presented here. In addition, results from a full raster observation on August 25, of a quiet sun region near the disc centre, westward of the coronal hole, are also presented and used as a quiet sun reference observation for that period.

5.2.1 The results from the Elephant's Trunk observations of the 26th August 1996

The following results are derived from composite series of four LIMB studies of the 26th (11:21-13:49 UT) and the CHBOPT2 study of the same day (Solar X=-62, Solar Y=72, 15:00-15:57 UT).

Figure 5.4 shows monochromatic images of the Elephant's Trunk on the 26th, when it was close to the meridian. A few characteristic features are of note. It is well-known that emission from both coronal lines and from He I (and He II) lines (in the network) is depressed in coronal holes. Figure 5.4 confirms this picture and also reveals that the cell centres in this coronal hole were somewhat elongated and enlarged, as seen at both chromospheric (He II) and transition region (O V) levels. At higher temperatures, the network pattern tends to disappear, and the emission has a more diffuse character. Emission from the hottest ion observed (Si XII) is completely absent in the coronal hole.

The scattered light

Figure 5.5 displays the 'background' level corresponding to the same observation, at the same wavelengths shown in Figure 5.4. Most of this scattered light (discussed in Chapter 3) is spatially-dependent, being more intense in the network regions (defined below).

The definition of cell-centre and network areas

The intensity of the O V 629.7 Å line has been used to distinguish between cell-centre and network areas (see, e.g., *Reeves*, 1976 for the technique, and *Gallagher et al.*, 1998, for a recent re-examination of the quiet sun cell and network structures) in order to produce consistently-defined average spectra of the regions examined, and to look for possible broad correlations of the supergranular structure with variations of the deduced parameters (temperature, density, and abundances).

This transition region line was chosen because its intensities in the network are not diminished inside coronal hole areas, unlike the chromospheric He lines, and because is one of

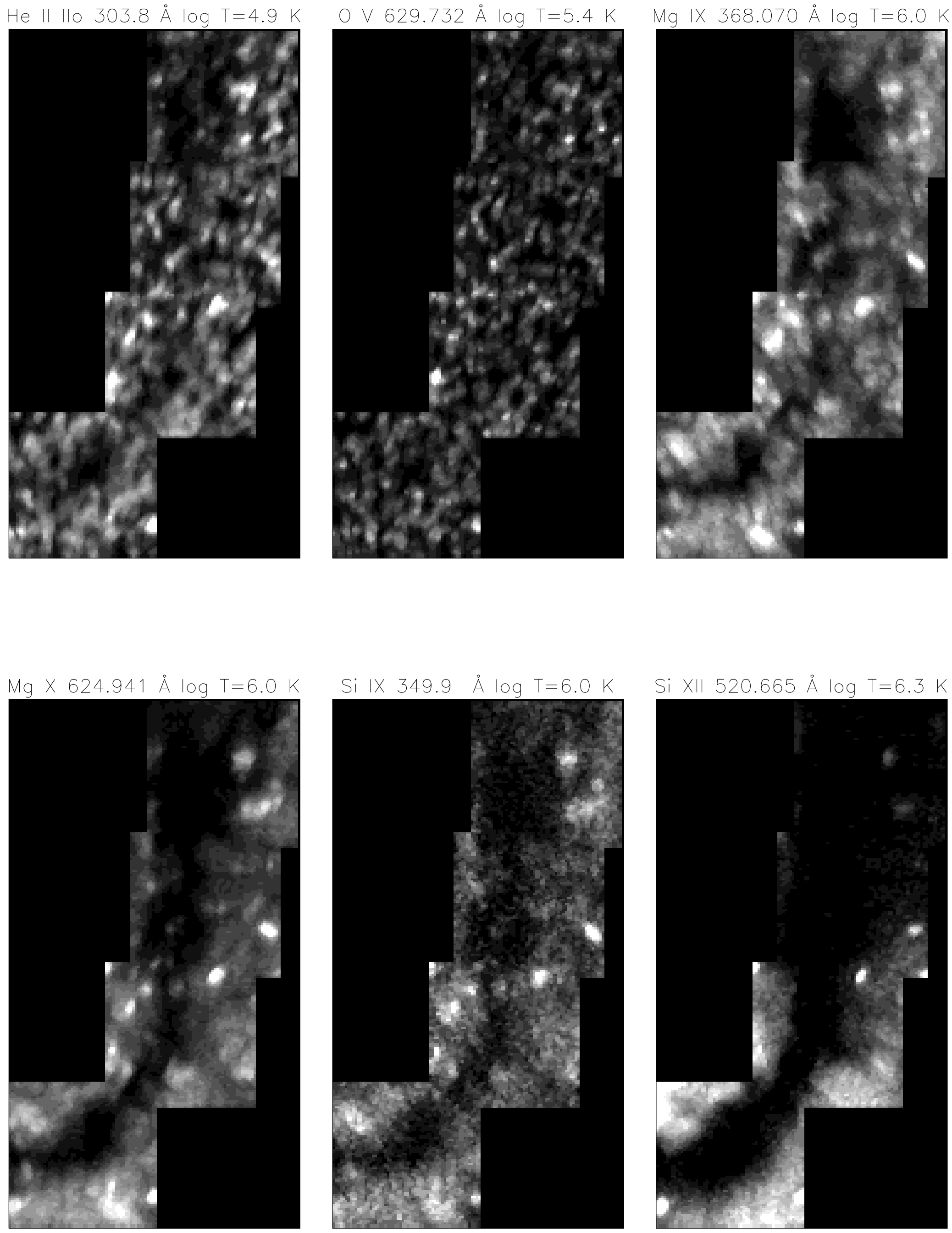

Figure 5.4: *The Elephant's Trunk in the solar corona imaged in EUV emission lines observed by CDS/SOHO on August 26, 1996.*

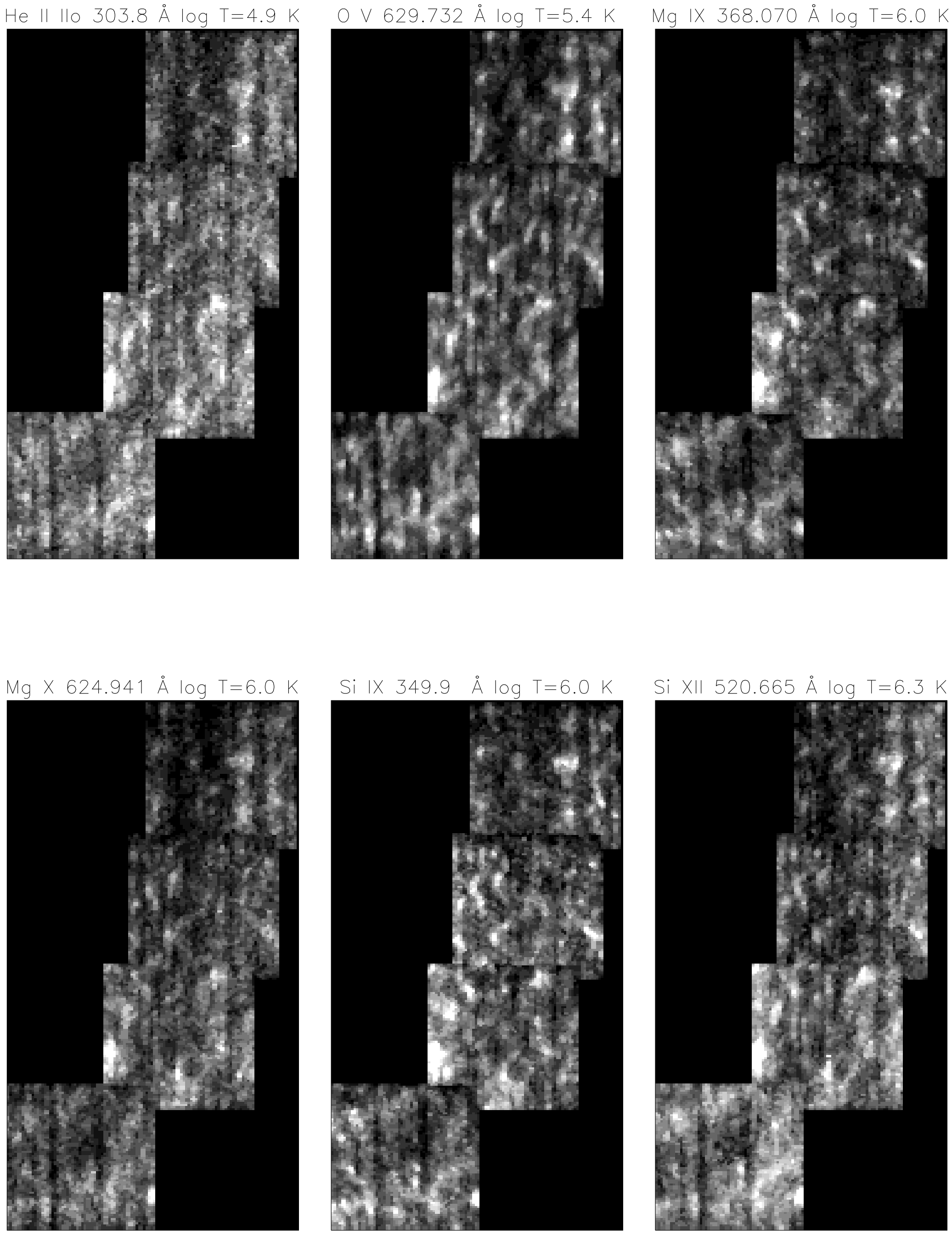

Figure 5.5: *The background level at the wavelengths corresponding to the lines indicated, in the same region shown in Figure 5.4.*

the brightest lines in the NIS spectra. The intensity distribution in O V has been fitted by a double Gaussian profile. Cell-centre (network) areas were defined as those regions having intensities less than (above) the value at the crossover of the two Gaussian profiles. This criterion has been applied to all the coronal hole and quiet sun observations analyzed. Figure 5.6 shows a histogram of the intensity over the whole of the mosaic area, and a visual representation of the cell-centre regions selected with the adopted criterion. It should be said that different choices of definitions of cell-centre and network regions lead to slightly different results.

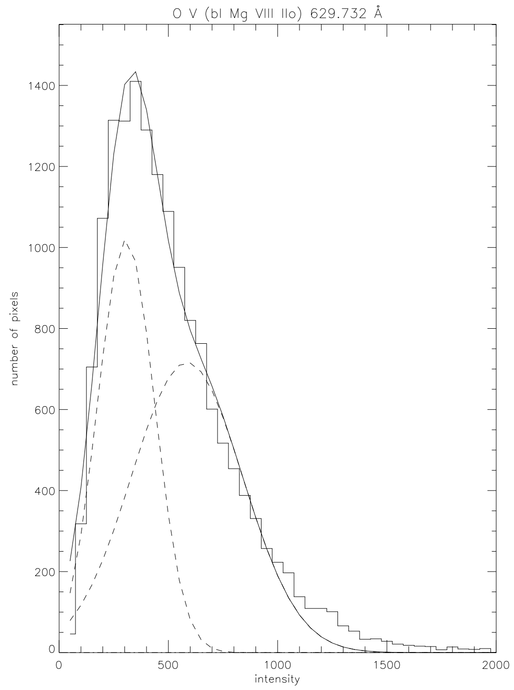

Figure 5.6: *The histogram of the O V 630 Å intensities from the August 26 1996, observation, showing the two-component gaussian fit used to define cell centre and network regions. The high-intensity tail represents localised brightenings in the network.*

The definition of coronal hole boundaries

It is difficult to unambiguously define coronal hole boundaries using EUV on-disc observations. Using intensities of coronal lines can be highly misleading, since the emission measure at any particular temperature along the line of sight can be expected to vary, and also abundance variations can affect the integrated intensity along the line of sight. An isothermal temperature map, on the other hand, shows much more clearly the boundaries of coronal holes. In the case of the Elephant's Trunk, the isothermal temperature map (Figure 5.7) clearly shows the extension of the polar hole down to the equator, and its continuity all the way from the north pole to the associated active region, as also shown by magnetograms.

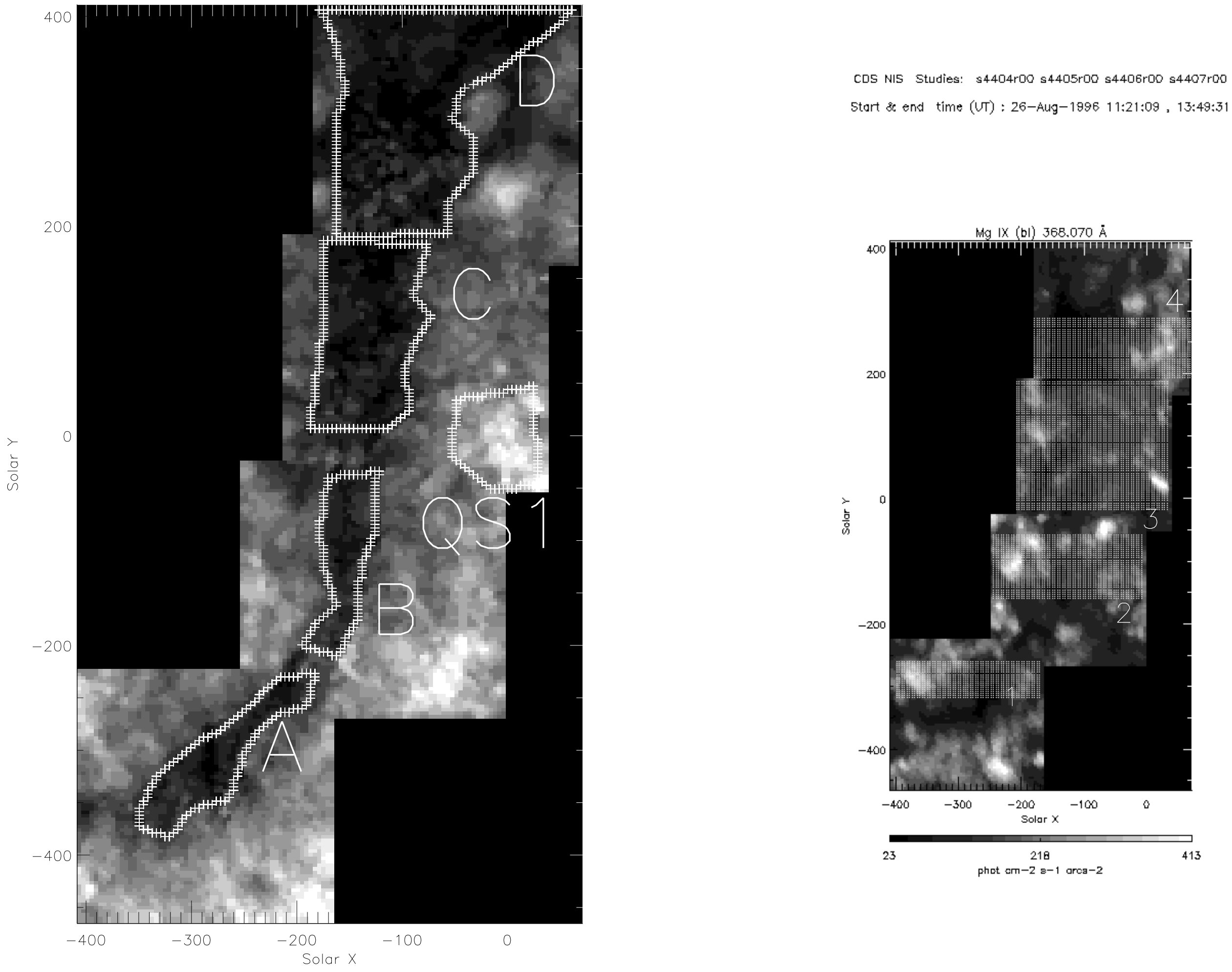

Figure 5.7: Left: an isothermal temperature map (Mg X 625 Å/ Mg IX 368 Å ratio) with the selected coronal hole areas, on August 26, 1996. Right: the Mg IX 368 Å image with the regions selected to get averaged E-W profiles.

Figure 5.7 shows the isothermal temperature map of the hole based on the [Mg X 624.9 Å/ Mg IX 368.0 Å] ratio. This image indicates a steep change in temperature at the boundaries of the hole. In this work, coronal hole areas were defined as regions with an isothermal temperature $T \leq 9.3 \text{x} 10^5$ K ($\log T \leq 5.97$). Other temperature ratios (e.g. Si XII/Si XI, Fe XII/Fe X) represent the coronal hole in a similar way. This Mg ratio was chosen because even inside the coronal hole both lines still have detectable intensities.

Since the coronal hole extended mainly along the N-S direction, regions near the equator were selected (see also Figure 5.7), and spectra were averaged along the N-S direction in order to increase the signal to noise and to produce intensity profiles across the hole (i.e. in the E-W direction). Figure 5.8 shows the two E-W intensity profiles (corresponding to the regions 2 and 3 in Figure 5.7) for the cell-centre areas in five different lines, together with the corresponding isothermal temperatures. The profile of the isothermal temperature shows that a log T value of 5.97 is a reasonable limit to use in defining the 'coldest' regions inside the hole (see also the temperatures derived from GIS lines, Figure 5.20). Similar temperature changes across the hole were found when looking at the other latitudes. The temperature on the eastern boundary of the hole was found in many places to be higher than on the west.

Using the Mg X/Mg IX intensity ratio to define coronal hole regions would bias any difference between coronal hole and quiet sun regions toward a temperature effect. However, this choice is in quite good agreement with the shape of the hole as seen in He I 10830 Å and YOHKOH images, that are usually used to trace the coronal hole boundaries.

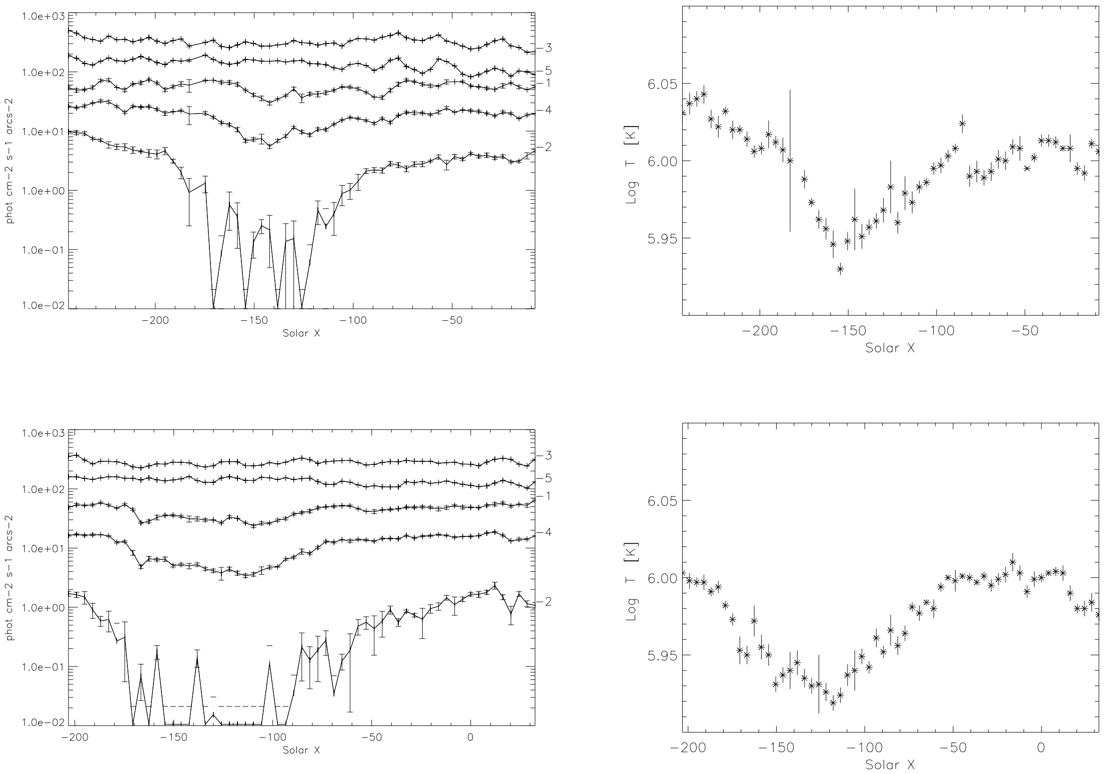

Figure 5.8: *Left: Intensity profiles across the coronal hole as deduced from cell-centre-averaged spectra of the regions 2 (above) and 3 (below) in Figure 5.7. (1) Mg IX 368. Å; (2) Si XII 520.7 Å; (3) He I 584.3 Å; (4) Mg X 625 Å; (5) O V 629.7 Å. Right: Profiles of the isothermal temperature derived from the Mg X 625 Å/ Mg IX 368 Å ratio. Note the decrease in the temperature.*

Figure 5.8 also shows that the cell-centre intensity in the He lines is almost unaltered. Similar studies over the network regions are also interesting, and show the well-known depression of the He lines inside coronal holes. There is also a tendency for transition

Table 5.1: *Electron Densities and Temperatures Deduced From the August 26, 1996, LIMB and CHBOPT2 Observations, for the Cell Centres and Network of the Selected Coronal Hole and Quiet Sun Areas. CC, cell centre; Net, network; CH, coronal hole; QS 1, quiet sun. Densities, deduced from the Si IX [349.9 Å/ 341.9 Å] and O IV [625.9 Å/ 608.4 Å] ratios are in cm^{-3}. Temperatures, deduced from the [Mg X 624.9 Å/ Mg IX 368.0 Å] ratio are in K. Intensities of a selection of lines are also shown, expressed as a proportion of the corresponding intensities seen in the quiet sun full raster observation of August 25, 1996.*

REGION	N_e (Si IX)	N_e (O IV)	T_e	He II	O V	Mg IX	Si XI
Mosaic CH A CC	2.8±.3 10^8	0.7±.1 10^{10}	8.95±.03 10^5	0.86	0.94	0.43	0.43
Mosaic CH B CC	1.7±.3 10^8	1.1±.4 10^{10}	9.06±.05 10^5	1.07	1.02	0.61	0.57
Mosaic CH C CC	2.2±.6 10^8	0.6±.1 10^{10}	8.8±.02 10^5	1.07	1.07	0.44	0.44
CHBOPT2 CH CC	1.6±.3 10^8	0.7±.1 10^{10}	8.57±.04 10^5	1.04	1.06	0.41	0.22
Mosaic CH D CC	2.0±0.5 10^8	0.6±.1 10^{10}	8.59±.03 10^5	0.87	1.0	0.40	0.37
Mosaic QS 1 CC	3.8±.5 10^8	1.2±.3 10^{10}	1.05±.02 10^6	1.0	0.85	0.58	0.96
Mosaic CH A Net	2.1±.5 10^8	0.5±.1 10^{10}	8.91±.05 10^5	0.69	0.91	0.43	0.47
Mosaic CH B Net	2.0±.7 10^8	0.7±.1 10^{10}	9.16±.05 10^5	0.80	0.94	0.63	0.57
Mosaic CH C Net	2.2±.3 10^8	0.5±.1 10^{10}	8.87±.04 10^5	0.86	1.06	0.49	0.49
CHBOPT2 CH Net	1.7±.5 10^8	0.5±.1 10^{10}	8.63±.04 10^5	0.72	0.93	0.38	0.19
Mosaic CH D Net	2.7±1. 10^8	0.5±.1 10^{10}	8.53±.03 10^5	0.66	0.94	0.38	0.39
Mosaic QS 1 Net	4.5±1. 10^8	0.5±.1 10^{10}	1.03±.04 10^6	0.94	0.84	0.74	0.94

region lines (O V) to have an increased intensity in both cell-centres and network (see also the results in Table 5.1). Also note the expansion of the coronal hole with height, as shown by the fact that higher-temperature lines show broader intensity depressions at the hole.

Figure 5.7 also indicates the four coronal hole regions (A, B, C, and D) that were selected to produce averaged spectra from the LIMB observations of the 26th of August. A region of quiet sun (QS 1; Figure 5.7) near Sun centre was chosen for comparison. This region does not necessarily represent the typical quiet sun, but on the other hand the notion of the so-called quiet sun has been radically changed by SOHO results. (Different averaged line intensities have been found from different quiet sun regions, and these differences can be quite large in particular for transition region lines in the network areas, because of the occurrence of repeated brightenings). All the quiet sun and coronal hole regions selected here were subdivided into cell-centre and network regions to enable separate measurement of the line intensities for each region to be made. The results are shown in Table 5.1.

Figure 5.9 shows the averaged spectra for the cell-centres of the coronal hole C region. Note how the line profiles are well defined even in this case, where intensities are very low, both in coronal lines (because of sampling inside a coronal hole), and in the other lines (because of sampling in the darker cell-centres).

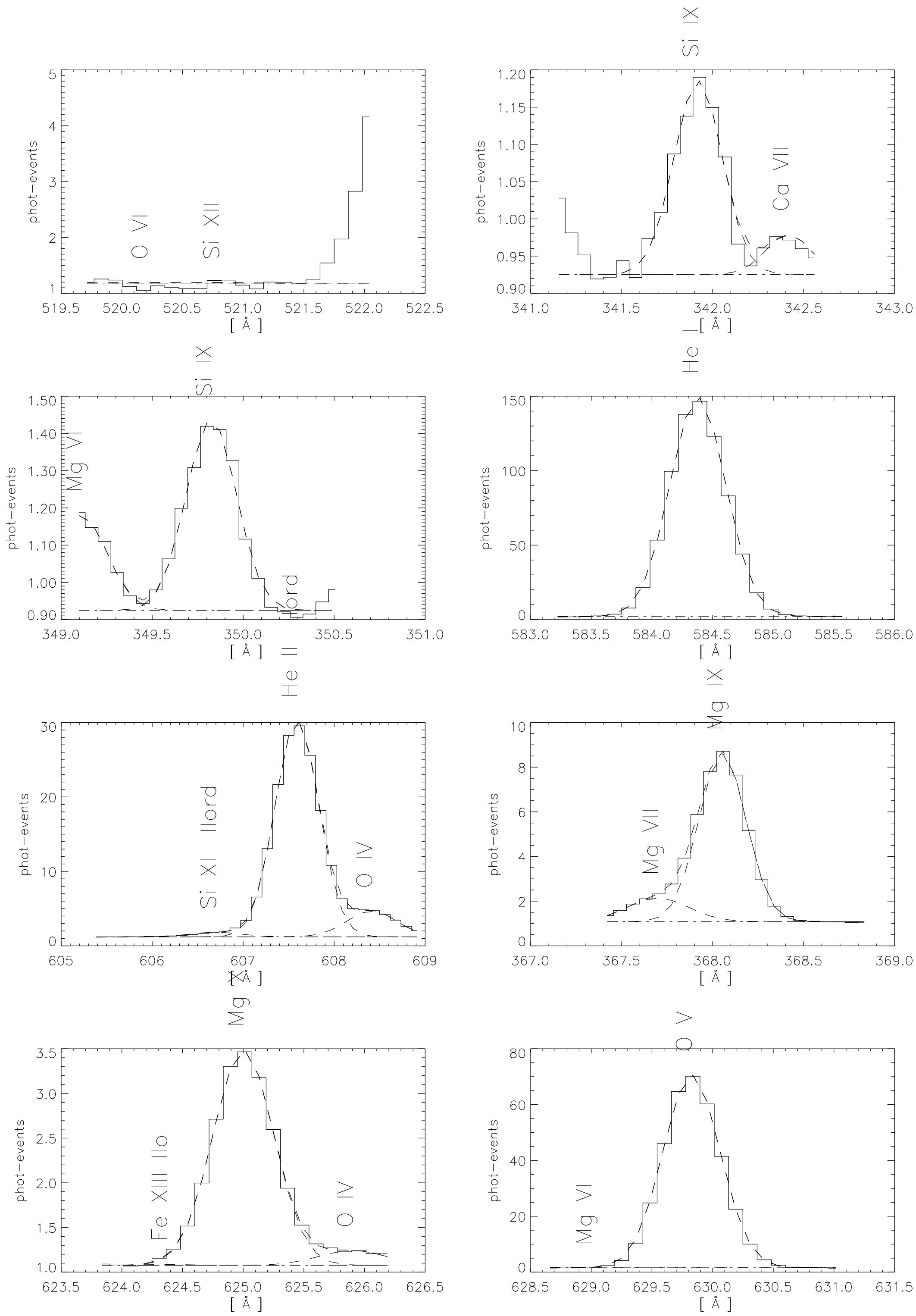

Figure 5.9: *The averaged spectra for the cell-centres of the coronal hole C region. – August 26, 1996.*

Table 5.1 also shows the results from the CHBOPT2 observation of August 26, which partly overlaps region C of the composite image.

Averaged coronal densities in the QS 1 region are about a factor of 2 higher than the coronal hole values . Coronal densities are not significantly different for network and cell-centre data, as one would expect, but at transition region heights the O IV ratio shows lower densities in the coronal hole areas, with a tendency to higher densities in the cell centres. While the quiet sun area QS 1 shows a temperature $T \simeq 1\text{x}10^6$ K, the coronal hole regions had temperatures $T \simeq 8.5 - 9\text{x}10^5$ K. Table 5.1 also shows the intensities of a few lines expressed relative to those in the quiet sun (full raster) observation of August 25 (see next section). The coronal lines Si XI 303.3 Å (second order) and Mg IX 368.0 Å are weaker by more than 50% inside the coronal hole. The transition region line O V 629.732 Å is slightly enhanced in the cell-centre regions inside the coronal hole, while the He II 303.8 Å (second order) line displays the well-known characteristic of decreased intensity in the coronal hole network, by 20-30%.

5.2.2 Results from the quiet sun reference observation - 1996, Aug 25

Before describing the results of the full diagnostic analysis performed on the coronal hole observations of Aug 27, results from the reference (full raster) quiet sun observation are now presented. This region was fairly homogeneous and very quiet. The NISAT observation on the Quiet Sun on 1996, Aug 25 was analyzed and cell-centre and network regions were selected following the same criterion previously described. Averaged spectra were then obtained, and line intensities derived.

The derived densities and temperatures are presented along with corresponding results for the Elephant's Trunk, in Table 5.4, below, for a more direct comparison. Averaged coronal densities are lower than in the region QS 1, while the isothermal temperature is about the same, around a million degrees. The [Mg VI 349.17 Å/ Ne VI 562.8 Å] ratio values shown in Table 5.4 indicate some differences in the elemental abundances between the cell centres and the network. This is confirmed by the Mg VII / Ne VII ratios.

DEM analyses were performed on the averaged cell-centre and network spectra, assuming a constant electron pressure of $4\text{x}10^{14}$ cm^{-3} K. The photospheric abundances of *Grevesse and Anders* (1991) in order to obtain a satisfactory fit were used initially, but some of the element abundances had to be modified (see Table 5.4 for the values adopted). Figure 5.10 shows the DEM distribution of the cell-centre quiet sun averaged spectrum.

Table 5.2: *A selection of lines of different ions, used for the DEM of the quiet sun averaged cell-centre region – 1996 August 27.*

Ion	λ_{th} (Å)	λ_{ob} (Å)	Transition	I_{ob}	I_{th}/I_{ob}	+/-	Det	log T_{eff}	log T_{max}	frac
C III	538.31	538.2	2s2p $^3P_2$ - 2s3s $^3S_1$	10.1	0.86	0.33	N 2	4.87	4.96	0.35
O II	538.32		2s22p3 $^2D_{3/2}$ - 2s2p4 $^2P_{3/2}$						4.87	0.33
C III	538.147		2s2p $^3P_1$ - 2s3s $^3S_1$						4.96	0.21
O III	599.597	599.6	2s22p2 $^1D_2$ - 2s2p3 $^1D_2$	24.9	1.17	0.19	N 2	5.05	5.06	
O IV	554.513	554.5	2s2 2p $^2P_{3/2}$ - 2s 2p2 $^2P_{3/2}$	82.4	0.98	0.12	N 2	5.26	5.27	
O IV	553.329	553.4	2s2 2p $^2P_{1/2}$ - 2s 2p2 $^2P_{3/2}$	14.3	1.12	0.24	N 2	5.26	5.27	
O IV	608.397	608.4	2s2 2p $^2P_{1/2}$ - 2s 2p2 $^2S_{1/2}$	13.6	0.90	0.40	N 2	5.26	5.27	
Ne IV	541.128	541.1	2s2 2p3 $^4S_{3/2}$ - 2s 2p4 $^4P_{1/2}$	1.9	1.03	0.93	N 2	5.29	5.27	
Ne IV	543.892	543.9	2s2 2p3 $^4S_{3/2}$ - 2s 2p4 $^4P_{5/2}$	5.7	1.04	0.52	N 2	5.29	5.27	
O V	629.73	629.8	2s2 $^1S_0$ - 2s.2p $^1P_1$	183.7	0.92	0.11	N 2	5.40	5.39	
Ne V	569.824	569.8	2s22p2 $^3P_1$ - 2s2p3 $^3D_2$	3.7	1.21	0.51	N 2	5.50	5.47	0.76
Ne V	569.753		2s22p2 $^3P_1$ - 2s2p3 $^3D_1$						5.47	0.24
Ne V	572.331	572.3	2s22p2 $^3P_2$ - 2s2p3 $^3D_3$	5.7	1.22	0.38	N 2	5.50	5.47	0.85
Ne V	572.098		2s22p2 $^3P_2$ - 2s2p3 $^3D_2$						5.47	0.14
Mg V	353.092	353.1	2p4 $^3P_2$ - 2s.2p5 $^3P_2$	3.9	0.56	0.40	N 1	5.54	5.47	
Ne VI	562.803	562.8	2s2 2p $^2P_{3/2}$ - 2s 2p2 $^2D_{5/2}$	10.3	1.12	0.25	N 2	5.68	5.63	
Ne VI	558.594	558.6	2s2 2p $^2P_{1/2}$ - 2s 2p2 $^2D_{3/2}$	7.3	0.94	0.28	N 2	5.70	5.63	0.88
Ne VII	558.609		2s2p $^3P_1$ - 2p2 $^3P_2$						5.72	0.12
Mg VI	349.168	349.1	2s2.2p3 $^2D_{5/2}$ - 2s.2p4 $^2D_{5/2}$	7.7	0.80	0.72	N 1	5.83	5.65	0.46
Mg VI	349.137		2s2.2p3 $^2D_{3/2}$ - 2s.2p4 $^2D_{3/2}$						5.65	0.38
Ne VII	561.728	561.7	2s2p $^3P_2$ - 2p2 $^3P_2$	3.2	0.92	0.49	N 2	5.85	5.72	0.83
Ne VII	561.378		2s2p $^3P_1$ - 2p2 $^3P_1$						5.72	0.17
Mg VII	367.674	367.7	2s22p2 $^3P_2$ - 2s2p3 $^3P_2$	19.3	0.83	0.46	N 1	5.92	5.81	0.77
Mg VII	367.683		2s22p2 $^3P_2$ - 2s2p3 $^3P_1$						5.81	0.23
Mg VII	365.234	365.2	2s22p2 $^3P_1$ - 2s2p3 $^3P_2$	10.3	0.96	0.87	N 1	5.93	5.81	0.37
Mg VII	365.176		2s22p2 $^3P_1$ - 2s2p3 $^3P_0$						5.81	0.34
Mg VII	365.243		2s22p2 $^3P_1$ - 2s2p3 $^3P_1$						5.81	0.27
Fe X	365.543	365.5	3s2.3p5 $^2P_{1/2}$ - 3s.3p6 $^2S_{1/2}$	13.3	1.18	0.76	N 1	5.95	6.04	0.70
Ne V	365.603		2s22p2 $^1D_2$ - 2s2p3 $^1P_1$						5.49	0.28
Mg X	609.793	609.8	1s2.(1s).2s $^2S_{1/2}$ - 1s2.(1s).2p $^2P_{3/2}$	85.7	1.34	0.19	N 2	5.97	6.04	0.80
O IV	609.829		2s2 2p $^2P_{3/2}$ - 2s 2p2 $^2S_{1/2}$						5.27	0.20
Mg VIII	339.006	339.0	2p $^2P_{3/2}$ - 2s.2p2 $^2S_{1/2}$	11.9	1.16	1.05	N 1	5.98	5.92	
Ca X	557.765	557.8	3s $^2S_{1/2}$ - 3p $^2P_{3/2}$	7.8	0.70	0.19	N 2	5.99	5.82	
Si VIII	319.826	319.8	2s22p3 $^4S_{3/2}$ - 2s2p4 $^4P_{5/2}$	53.0	1.34	0.83	N 1	6.00	5.91	
Mg IX	368.07	368.0	2s2 $^1S_0$ - 2s.2p $^1P_1$	176.2	0.97	0.13	N 1	6.02	5.98	
Si IX	349.873	349.8	2s22p2 $^3P_2$ - 2s2p3 $^3D_3$	33.6	1.13	0.59	N 1	6.04	6.02	0.84
Si IX	349.794		2s22p2 $^3P_2$ - 2s2p3 $^3D_2$						6.03	0.16
Fe X	345.723	345.7	3s2.3p5 $^2P_{3/2}$ - 3s.3p6 $^2S_{1/2}$	23.1	1.14	0.92	N 1	6.04	6.04	
Si IX	341.949	341.9	2s22p2 $^3P_0$ - 2s2p3 $^3D_1$	16.7	1.01	0.92	N 1	6.04	6.04	
Mg X	624.941	625.0	1s2.(1s).2s $^2S_{1/2}$ - 1s2.(1s).2p $^2P_{1/2}$	30.4	1.55	0.33	N 2	6.05	6.04	
Fe XI	352.662	352.6	3s2.3p4 $^3P_2$ - 3s.3p5 $^3P_2$	31.4	1.03	0.63	N 1	6.07	6.11	
Fe XI	369.153	369.1	3s2.3p4 $^3P_1$ - 3s.3p5 $^3P_2$	8.6	1.13	0.83	N 1	6.07	6.11	
Al X	332.789	332.8	2s2 $^1S_0$ - 2s.2p $^1P_1$	22.0	0.88	0.79	N 1	6.07	6.10	
Si X	356.012	356.0	2p $^2P_{3/2}$ - 2s.2p2 $^2D_{5/2}$	21.5	1.05	0.95	N 1	6.07	6.12	0.76
Si X	356.05		2p $^2P_{3/2}$ - 2s.2p2 $^2D_{3/2}$						6.14	0.24
Si X	347.403	347.4	2p $^2P_{1/2}$ - 2s.2p2 $^2D_{3/2}$	37.3	1.04	0.62	N 1	6.08	6.14	
Fe XII	352.106	352.1	3s2.3p3 $^4S_{3/2}$ - 3s.3p4 $^4P_{3/2}$	22.1	0.78	0.61	N 1	6.09	6.16	
Fe XII	346.852	346.8	3s2.3p3 $^4S_{3/2}$ - 3s.3p4 $^4P_{1/2}$	11.5	0.75	0.68	N 1	6.09	6.16	
Fe XII	364.467	364.4	3s2.3p3 $^4S_{3/2}$ - 3s.3p4 $^4P_{5/2}$	31.3	0.78	0.27	N 1	6.10	6.16	
Fe XIII	348.183	348.1	3s2 3p2 $^3P_0$ - 3s 3p3 $^3D_1$	10.5	1.19	1.08	N 1	6.13	6.21	
Fe XVI	360.761	360.6	3s $^2S_{1/2}$ - 3p $^2P_{1/2}$	2.5	0.79	0.71	N 1	6.34	6.34	

The lines used in the *DEM* analysis were formed over a wide range of temperatures and were from many different ions. Table 5.2 shows a selection of the lines used for the *DEM* analysis. Almost all the intense lines in both NIS 1 and NIS 2 detectors are well fitted, within a 20% accuracy, which is a remarkable result, considering the uncertainties in the calculations of the line intensities, in the atomic physics calculations and in the calibration.

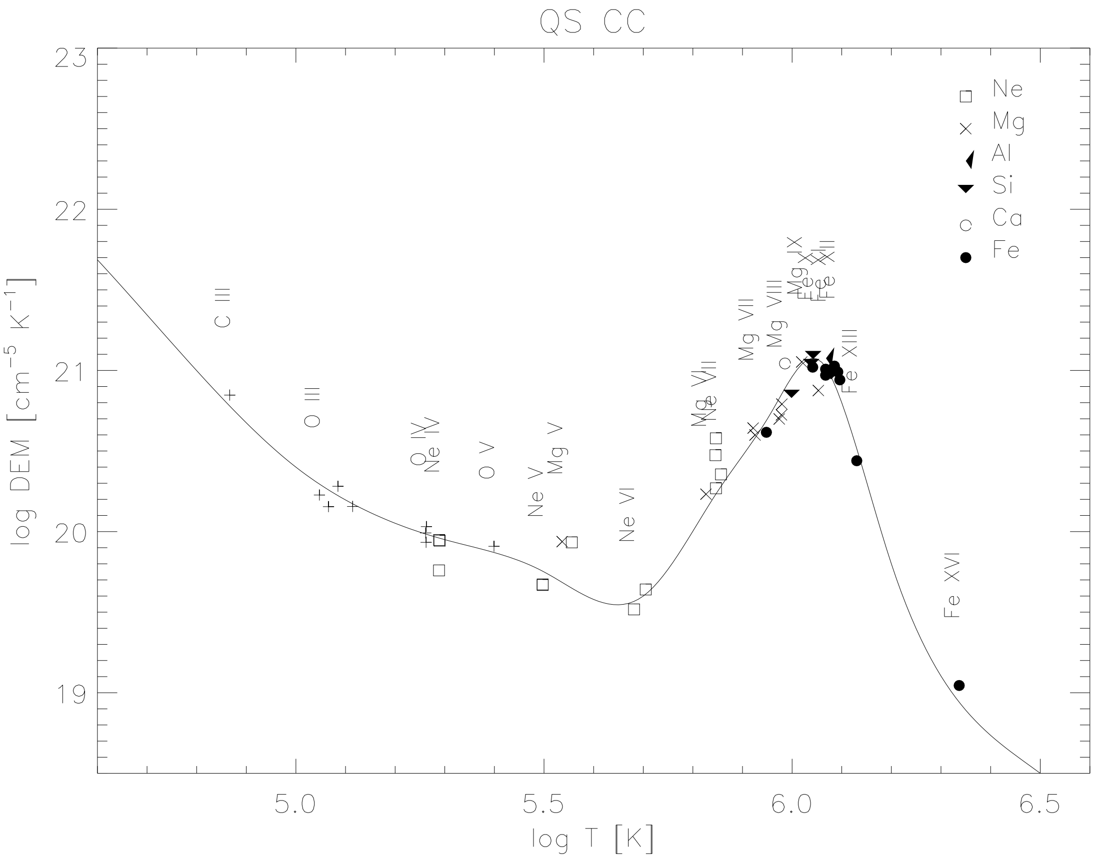

Figure 5.10: *The DEM distribution of the full raster quiet sun cell-centres region on August 25, 1996.*

This quiet sun DEM distribution is similar to those derived by previous authors (e.g., *Raymond and Doyle, 1981b; Brosius et al., 1996; Mason et al.,* 1997, *Doschek*, 1997). The DEM curve between log $T = 5.0$ and log $T = 5.4$ is constrained by O III, O IV, and O V lines. The DEM values between log $T = 5.3$ and log $T = 5.8$ are also well constrained by bright NIS 2 lines of Ne IV, Ne V, Ne VI, and Ne VII. The DEM distribution here is therefore independent of relative O/Ne element abundances. The relative O/Ne abundance was in fact constrained by O IV and Ne IV lines: The Ne abundance was increased by a factor 1.6 (0.2 dex), relative to O. The abundances of the low-FIP elements were then scaled with the Ne value.

The temperature of the coronal peak of the DEM distribution is in agreement with the isothermal temperature deduced from the [Mg X 624.9 Å/ Mg IX 368.0 Å] ratio (Table 5.4). This shows that the Sun at that time was very quiet, with a much lower emission at temperatures above a million degrees, compared to previous analyses (e.g., *Raymond and Doyle*, 1981b).

For consistency, the same set of lines was used for the DEM analyses of the quiet sun network and the coronal hole regions, described below, The DEM distribution of the quiet sun network is shown in Figure 5.11. The shape and position of the coronal peaks in the cell-centre and network quiet sun DEM distributions are similar, whereas the network DEM shows much higher emission measures in the whole of the transition region, as expected. The two DEM distributions are directly compared in Figure 5.21, below.

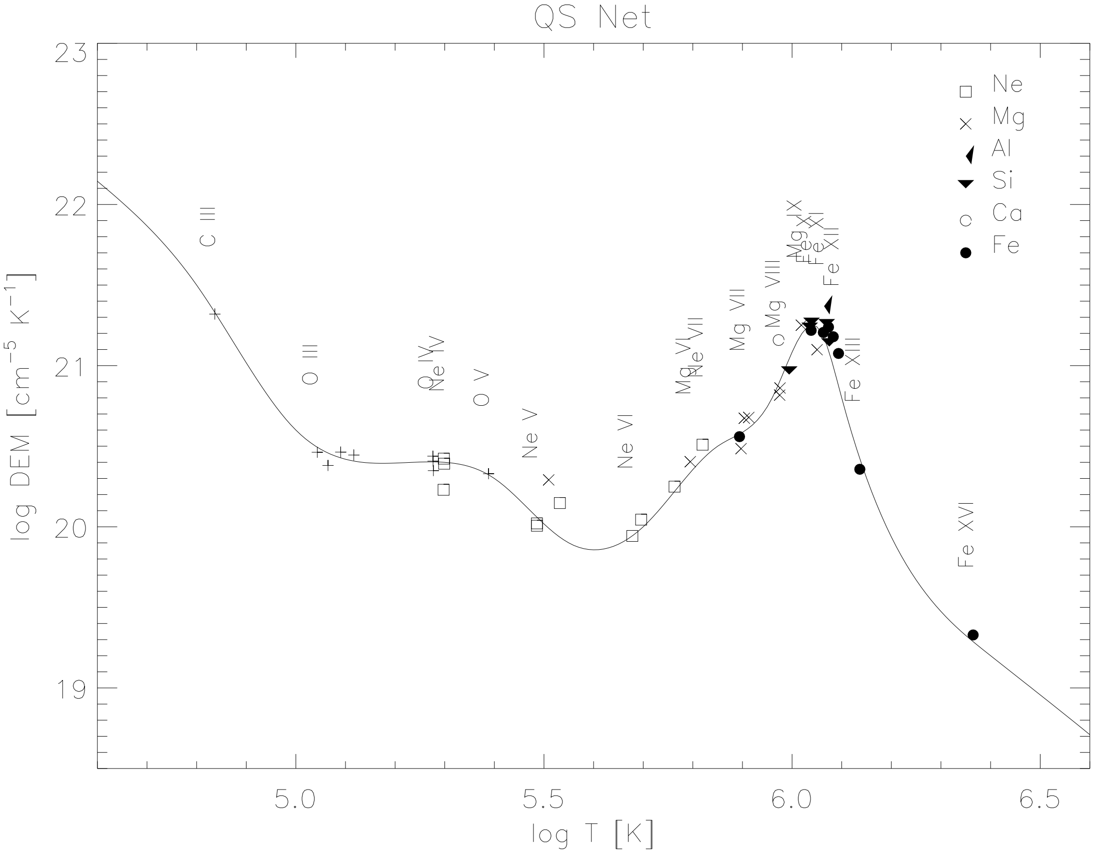

Figure 5.11: *The DEM distribution of the full raster quiet sun network region on August 25, 1996.*

5.2.3 Coronal hole and plume densities, temperatures and abundances - 1996 August 27

Results based on the analysis of the CHBOPT2, the NISAT_S5 and one of the G2AL/v2 studies of the 27th August are presented here (see Figure 4.6 for the pointing of these CDS observations). The GIS E-W raster (fits file s4431r00) was the first one to be run, starting at 06:32 UT, at Solar Y = 81″, very close to the disc centre. This study used the 4″x4″slit and 400s exposures. Then, after a second GIS E-W scan, the full NIS spectrum (NISAT_S5 study, Solar X=107″, Solar Y=71″, 11:01-12:08 UT) was performed, and then the CHBOPT2 observation followed (Solar X=142″, Solar Y=71″, 12:13-13:10 UT). The

CHBOPT2 and NISAT_S5 rasters of the 27th therefore pointed at the same region in the N-S direction, but were shifted E-W, so as to have an overlap between the two.

Figure 5.12 shows monochromatic images in a few selected lines from the CHBOPT2 observation. The full spectrum (NISAT_S5) observation has been used to perform a DEM analysis of the Elephant's Trunk (see below).

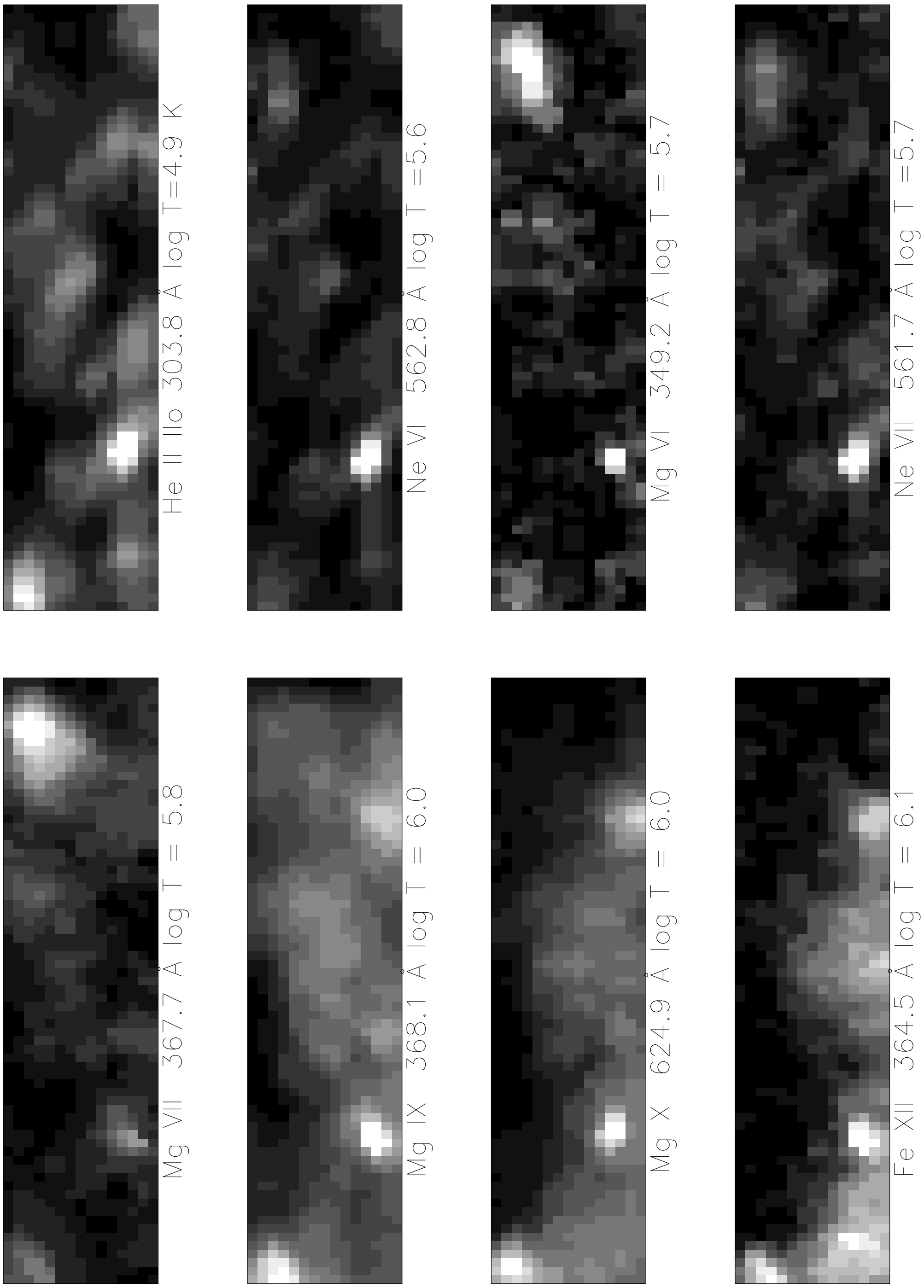

Figure 5.12: Monochromatic images of the CHBOPT2 observation on August 27, 1996.

Examination of Figure 5.12 shows that the network signature is evident in the transition region lines and tends to disappear when lines that form at higher temperatures are examined. The coronal hole boundary is clearly visible in the Fe XII image.

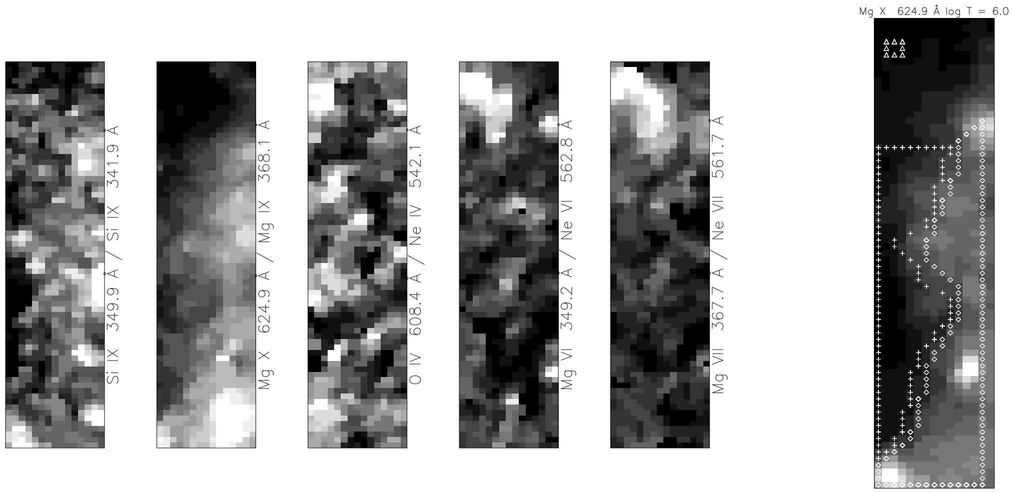

Figure 5.13: *Left: ratio images of the CHBOPT2 observation on August 27, 1996, showing density ratios (Si IX); temperature ratio (Mg X / Mg IX); and abundance ratios. Right: selected regions from which average spectra were extracted (see Figure 5.14). Triangles refer to the plume region, crosses refer to the coronal hole region, and diamonds refer to the west boundary region.*

Figure 5.13 shows density, temperature, and abundance maps of the same region. Small-scale inhomogeneities are present in all the ratio images, but some large-scale patterns are recognizable. At coronal levels (Si IX), a decrease in density toward the 'deepest' region of the coronal hole is evident. The Mg X / Mg IX image shows a clear temperature decrease in the coronal hole region, corresponding to the darker area in the Fe XII image. The whole eastward region (left in the images) in the raster could therefore be interpreted as a coronal hole region, with the upper part showing lower temperatures than the rest of the coronal hole.

In the low coronal line Mg IX 368.0 Å (Figure 5.12), a diffuse emission is present in the upper part of the image, also visible in the EIT 195 Å image (Figure 4.6) but not in the higher temperature lines Mg X 624.9 Å and Fe XII 364.5 Å observed by CDS. In the same region, the abundance maps indicate a strong enhancement in the Mg/Ne relative abundance, compared to the remainder of the coronal hole, and a bright feature can be seen in the same position in the Mg VI and Mg VII images (Figure 5.12). The Mg/Ne enhancement is typical of plumes observed in Skylab data, suggesting that this feature is a small plume, directed almost toward the observer (see later).

At the base (higher Solar Y) of the plume a (small) increase in the O IV/Ne IV ratio suggests that some of the Mg/Ne enhancement is due to a low Ne abundance relative to O. The variations of the [Mg VI 349.17 Å/ Ne VI 562.8 Å] ratio in the rest of the coronal hole area suggests a possible enhancement of Mg/Ne in cell-centre regions over those in the network (cf. He II intensities in Figure 5.12, which show the supergranular structure).

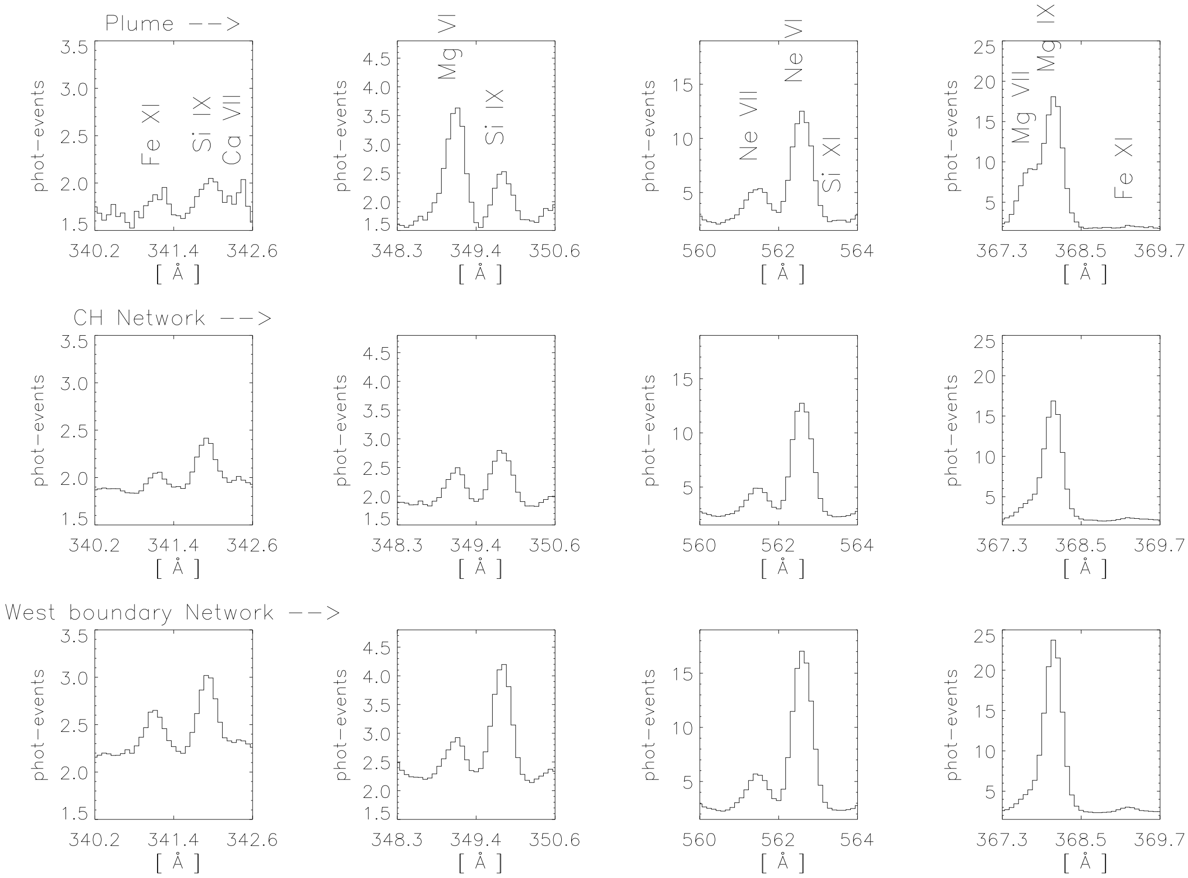

Figure 5.14: *Averaged spectra of the selected regions (see Figure 5.13) of the CHBOPT2 observation on August 27, 1996: (top) plume, (middle) coronal hole network, and (bottom) west boundary (quiet sun) network. Note the same intensity scale and the enhancements in the Mg VI and Mg VII lines in the plume.*

Figure 5.13 (right hand image) also shows some selected regions of the CHBOPT2 study: a small area centred on the base of the plume; a coronal hole region; and a nearby quiet sun region on the western boundary of the hole. Figure 5.14 shows averaged line profiles in a few selected lines, for these three regions.

The enhancements in the Mg VI and Mg VII lines in the plume region are particularly evident, as compared, for example, with Ne VI and Mg IX. The most striking differences between the plume and the coronal hole are seen in the Mg IX / Mg VII blend at 368 Å. This indicates a different plasma temperature distribution at the base of the plume, with large emission measures at Mg VII temperatures, compared with the nearby regions.

The fact that Ne VI and Ne VII emissions in the plume are very similar to those in the coronal hole then suggests a variation of the Mg/Ne abundance. This is studied below with a DEM analysis.

Coronal hole regions excluding the plume have also been selected and then subdivided into coronal hole cell centre and network in the usual way. Since the plume was partly visible in the NISAT_S5 field of view, it was possible to perform a DEM analysis based on all the NIS lines seen at the base of the plume. This is also presented below. Results based on the line intensities of the CHBOPT2 observation are presented in *Del Zanna and Bromage* (1999a). Table 5.4 shows the results for the plume and the coronal hole regions, as derived from the NISAT_S5 observation (together with the results of the quiet sun observation). The plume had an isothermal temperature $T \simeq 8\text{x}10^5$ K, lower than the values found in the average coronal hole regions ($T = 8.3 - 9\text{x}10^5$ K). The plume also had a higher value (1.04) for the [Mg VI 349.17 Å/ Ne VI 562.8 Å] ratio, as compared with the coronal hole values ($\simeq$ 0.4) and quiet sun values (0.54–0.75).

This 'plume' feature shows all the characteristics of polar plumes seen on-disc with CDS, as shown in Chapter 6 of this thesis. These characteristics include: lower temperature than the ambient coronal hole region; visibility only in lines emitted in a restricted range of temperatures; and enhanced Mg/Ne relative abundance. All this evidence supports the hypothesis that this feature is indeed a low-latitude plume. **This is the first identification of a low-latitude coronal hole plume** based on spectroscopic analysis. The results support the conclusions of previous authors (who based their conclusions on morphological characteristics) that plumes exist in low-latitude coronal holes as well as in polar holes (e.g., *Wang and Sheeley*, 1995a).

The spectra and DEM of the Elephant's Trunk coronal hole

NISAT_S5 spectra were spatially averaged over the coronal hole regions, and subdivided into cell-centre areas and network in the usual manner. A DEM analysis was then performed using all the measured NIS line intensities. (Figures D.1 and D.2 show as an example the full NIS averaged spectra for the network region). Note that even with long exposures (150s), the wider $4''$slit, and spatial averaging, the signal is still quite low. All the high-temperature lines are either very weak or absent.

For the DEM analyses on the network and cell-centre averaged spectra, a constant electron pressure of $2\text{x}10^{14}$ cm^{-3} K has been assumed. Table 5.4 (below) shows the abundances that were obtained from these DEM analysis. The resulting DEM distributions are shown in Figures 5.15 and 5.16, and Table 5.3 lists some of the lines used for the DEM

and abundance analysis for the network region. Note from Table 5.3 how all lines are well represented, except for Mg V (only one is shown in Table). This confirms the problem with the Mg V already noted in this thesis, and also present in the SERTS-89 spectra.

Note from Table 5.4 that the Ne abundance was slightly increased, compared to the photospheric value, but that on the other hand all the low-FIP elements had abundances slightly lower than photospheric (except Ca). Note from Figure 5.15 the very low emission measure values at high temperatures. The same figure shows the DEM_L values of the same lines. These confirm the very low emission measures at the highest temperatures, and the validity of the adopted relative abundances (because of the small scatter of points).

Table 5.3: *A selection of lines of different ions, used for the DEM analysis of the coronal hole averaged network region – 27th August 1996.*

Ion	λ_{th} (Å)	λ_{ob} (Å)	Transition	I_{ob}	I_{th}/I_{ob}	+/-	Det	log T_{eff}	log T_{max}	frac
O II	538.32	538.3	2s22p3 $^2D_{3/2}$ - 2s2p4 $^2P_{3/2}$	18.7	1.11	0.16	N 2	4.83	4.87	0.39
C III	538.31		2s2p $^3P_2$ - 2s3s $^3S_1$						4.96	0.32
C III	538.147		2s2p $^3P_1$ - 2s3s $^3S_1$						4.96	0.19
O III	599.597	599.7	2s22p2 $^1D_2$ - 2s2p3 $^1D_2$	55.5	1.03	0.11	N 2	5.03	5.06	
N III	374.434	374.5	2s2 2p $^2P_{3/2}$ - 2s2 3d $^2D_{5/2}$	5.0	0.95	0.76	N 1	5.08	5.09	0.34
O III	374.435		2s22p2 $^3P_2$ - 2s22p3s $^3P_1$						5.11	0.34
O III	374.33		2s22p2 $^3P_1$ - 2s22p3s $^3P_0$						5.11	0.28
O IV	554.513	554.6	2s2 2p $^2P_{3/2}$ - 2s 2p2 $^2P_{3/2}$	171.7	0.94	0.10	N 2	5.28	5.27	
Ne IV	543.892	544.0	2s2 2p3 $^4S_{3/2}$ - 2s 2p4 $^4P_{5/2}$	10.0	0.95	0.16	N 2	5.30	5.27	
O V	629.73	629.9	2s2 $^1S_0$ - 2s.2p $^1P_1$	391.5	0.98	0.10	N 2	5.39	5.39	
Ne V	572.331	572.4	2s22p2 $^3P_2$ - 2s2p3 $^3D_3$	9.8	1.17	0.15	N 2	5.49	5.47	0.86
Ne V	572.098		2s22p2 $^3P_2$ - 2s2p3 $^3D_2$						5.47	0.14
Mg V	353.092	353.1	2p4 $^3P_2$ - 2s.2p5 $^3P_2$	5.2	0.47	0.34	N 1	5.54	5.47	
Ne VI	562.803	562.9	2s2 2p $^2P_{3/2}$ - 2s 2p2 $^2D_{5/2}$	18.3	1.09	0.13	N 2	5.71	5.63	
Ne VI	558.594	558.7	2s2 2p $^2P_{1/2}$ - 2s 2p2 $^2D_{3/2}$	12.1	1.00	0.13	N 2	5.73	5.63	0.85
Ne VII	558.609		2s2p $^3P_1$ - 2p2 $^3P_2$						5.72	0.15
Mg VI	349.168	349.1	2s2.2p3 $^2D_{5/2}$ - 2s.2p4 $^2D_{5/2}$	6.6	1.10	0.98	N 1	5.81	5.65	0.51
Mg VI	349.137		2s2.2p3 $^2D_{3/2}$ - 2s.2p4 $^2D_{3/2}$						5.65	0.41
Ne VII	561.728	561.8	2s2p $^3P_2$ - 2p2 $^3P_2$	5.1	1.01	0.18	N 2	5.83	5.72	
Mg VII	367.674	367.7	2s22p2 $^3P_2$ - 2s2p3 $^3P_2$	18.2	1.14	0.52	N 1	5.88	5.81	0.76
Mg VII	367.683		2s22p2 $^3P_2$ - 2s2p3 $^3P_1$						5.81	0.23
Mg VII	365.234	365.2	2s22p2 $^3P_1$ - 2s2p3 $^3P_2$	12.5	1.00	0.57	N 1	5.88	5.81	0.37
Mg VII	365.176		2s22p2 $^3P_1$ - 2s2p3 $^3P_0$						5.81	0.35
Mg VII	365.243		2s22p2 $^3P_1$ - 2s2p3 $^3P_1$						5.81	0.27
Ca X	557.765	557.9	3s $^2S_{1/2}$ - 3p $^2P_{3/2}$	4.7	0.95	0.18	N 2	5.90	5.82	
Mg VIII	339.006	339.0	2p $^2P_{3/2}$ - 2s.2p2 $^2S_{1/2}$	10.1	1.05	0.75	N 1	5.92	5.92	
Mg IX	368.07	368.1	2s2 $^1S_0$ - 2s.2p $^1P_1$	76.6	0.92	0.14	N 1	5.96	5.98	
Si IX	349.873	349.9	2s22p2 $^3P_2$ - 2s2p3 $^3D_3$	8.2	1.25	0.93	N 1	5.98	6.02	0.81
Si IX	349.794		2s22p2 $^3P_2$ - 2s2p3 $^3D_2$						6.03	0.19
Fe X	345.723	345.7	3s2.3p5 $^2P_{3/2}$ - 3s.3p6 $^2S_{1/2}$	8.4	0.93	0.83	N 1	5.99	6.04	
Si IX	341.949	342.0	2s22p2 $^3P_0$ - 2s2p3 $^3D_1$	6.4	0.99	0.90	N 1	5.99	6.04	
Mg X	624.941	625.0	1s2.(1s).2s $^2S_{1/2}$ - 1s2.(1s).2p $^2P_{1/2}$	7.3	1.52	0.25	N 2	6.02	6.04	
Fe XI	369.153	369.3	3s2.3p4 $^3P_1$ - 3s.3p5 $^3P_2$	2.0	1.06	0.96	N 1	6.05	6.11	
Al X	332.789	332.8	2s2 $^1S_0$ - 2s.2p $^1P_1$	8.5	0.75	0.68	N 1	6.05	6.09	
Fe XI	352.662	352.7	3s2.3p4 $^3P_2$ - 3s.3p5 $^3P_2$	7.2	0.96	0.87	N 1	6.05	6.11	
Fe XII	364.467	364.5	3s2.3p3 $^4S_{3/2}$ - 3s.3p4 $^4P_{5/2}$	6.9	0.67	0.60	N 1	6.11	6.16	
Fe XII	346.852	347.0	3s2.3p3 $^4S_{3/2}$ - 3s.3p4 $^4P_{1/2}$	2.4	0.69	0.62	N 1	6.11	6.16	
Fe XIII	348.183	348.1	3s2 3p2 $^3P_0$ - 3s 3p3 $^3D_1$	2.8	1.10	1.00	N 1	6.16	6.20	
Fe XVI	360.761	360.6	3s $^2S_{1/2}$ - 3p $^2P_{1/2}$	1.7	0.76	0.69	N 1	6.38	6.34	

The cell-centre *DEM* distribution (Figure 5.16) also shows very low emission measures.

The coronal hole emission measures are directly compared in Figure 5.21, and discussed below.

The DEM of the low-latitude plume

A spatially averaged NISAT_S5 spectrum of a small region at the base of the plume was obtained and used for a *DEM* analysis. The results are shown in Figure 5.17 and in Table 5.4, where the adopted relative abundances can be found. The same set of spectral lines was used. A constant electron pressure of 2x10^{14} cm^{-3} K was assumed for the calculation of the contribution functions. As in the previous cases, the relative O/Ne abundance is constrained by O IV and Ne IV lines. This time, the O/Ne abundance has photospheric values. Mg VI/Ne VI and Mg VII/Ne VII lines were used to constrain the Mg/Ne abundance, and consequently also all the other low-FIP elements. A small FIP bias effect was found.

This plume showed an almost isothermal distribution at coronal heights, with a peak in the DEM at $T \simeq 7.7 \cdot 10^5$ K, close to the isothermal temperatures deduced from line ratios. The largest emission measures are thus at upper transition region temperatures (Mg VII, Ca X, Mg VIII), which explains why plumes are most clearly seen in lines emitted at those temperatures. A direct comparison with the other *DEM* distributions is presented in Figure 5.21, and discussed below.

The GIS E-W scan across the hole: abundance variations

Figure 5.18 shows the intensities of twenty lines from the GIS E-W scan across the hole. The intensities of the lower transition region lines (upper row) delineate the network and cell centre areas, and these tend to be less evident in the lines emitted at higher temperatures (lower rows). The low intensities inside the coronal hole are particularly evident for the hottest lines. While the eastward (left) part of this scan was in quiet sun, the westward (right hand end) is still partly in the coronal hole.

The thermal distribution inside the hole is different from that of the quiet sun, with intensities of the hottest lines being more depressed than those of the cooler ones (Fe XII/Fe X; Fe X/Fe IX), indicating much lower emission measures of the hotter lines inside the hole. The ratios of lines emitted by ions of different elements, but that have similar contribution functions, give an indication of possible abundance variations, as already discussed. GIS can detect many more lines useful for element abundance studies than can NIS.. Some examples are shown here in Figure 5.19. While some of the elements show constant relative abundance, (e.g. Mg and Si), others show large variations that follow

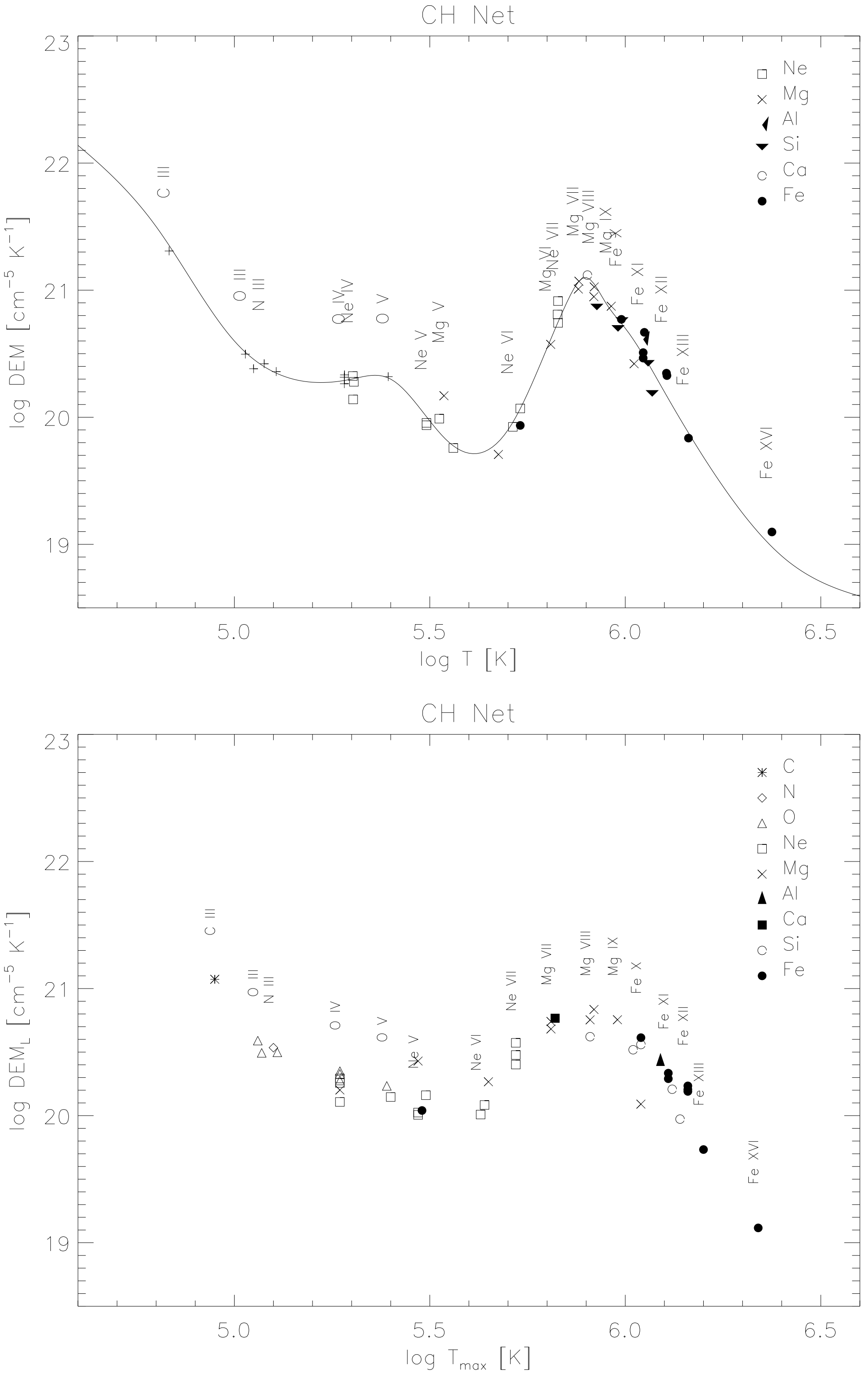

Figure 5.15: *The DEM distribution for the coronal hole network (CH Net) on August 27, 1996 (above), and the corresponding DEM_L values, plotted at the temperature $T_{\max}$.*

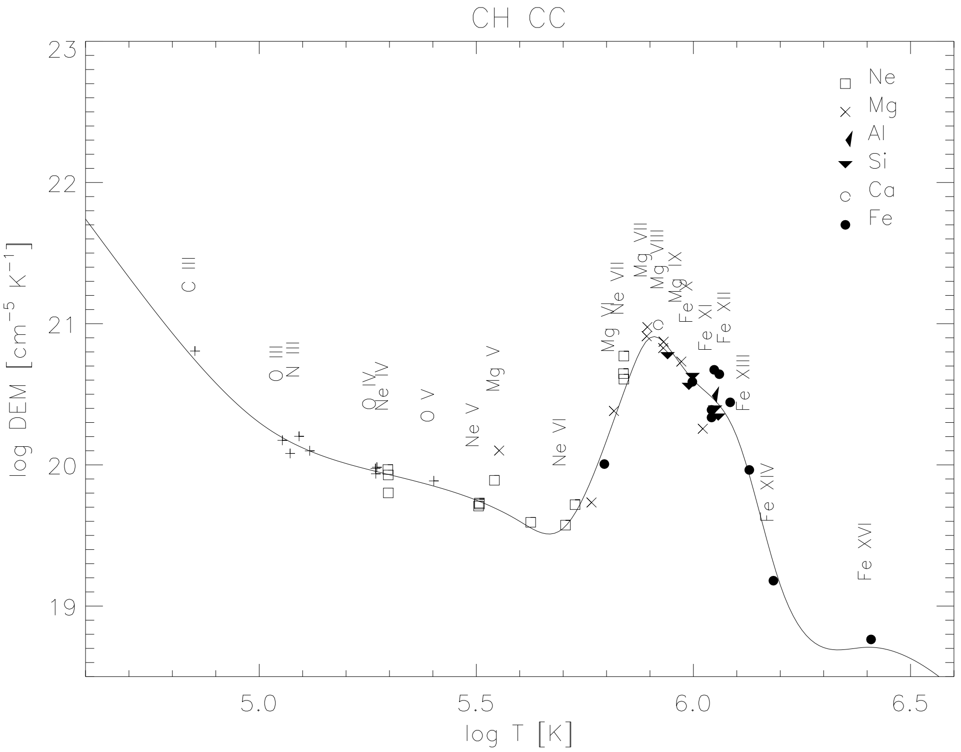

Figure 5.16: *The DEM distribution of the coronal hole cell-centre (CH CC) on August 27, 1996.*

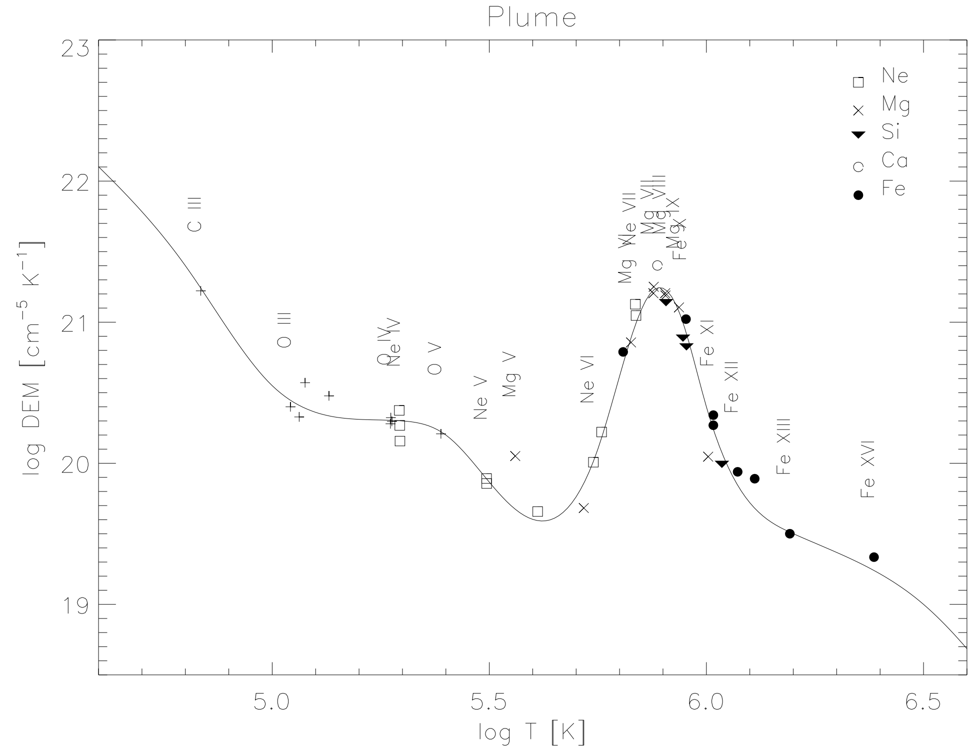

Figure 5.17: *The DEM distribution of the low-latitude plume in the Elephant's Trunk – August 27, 1996.*

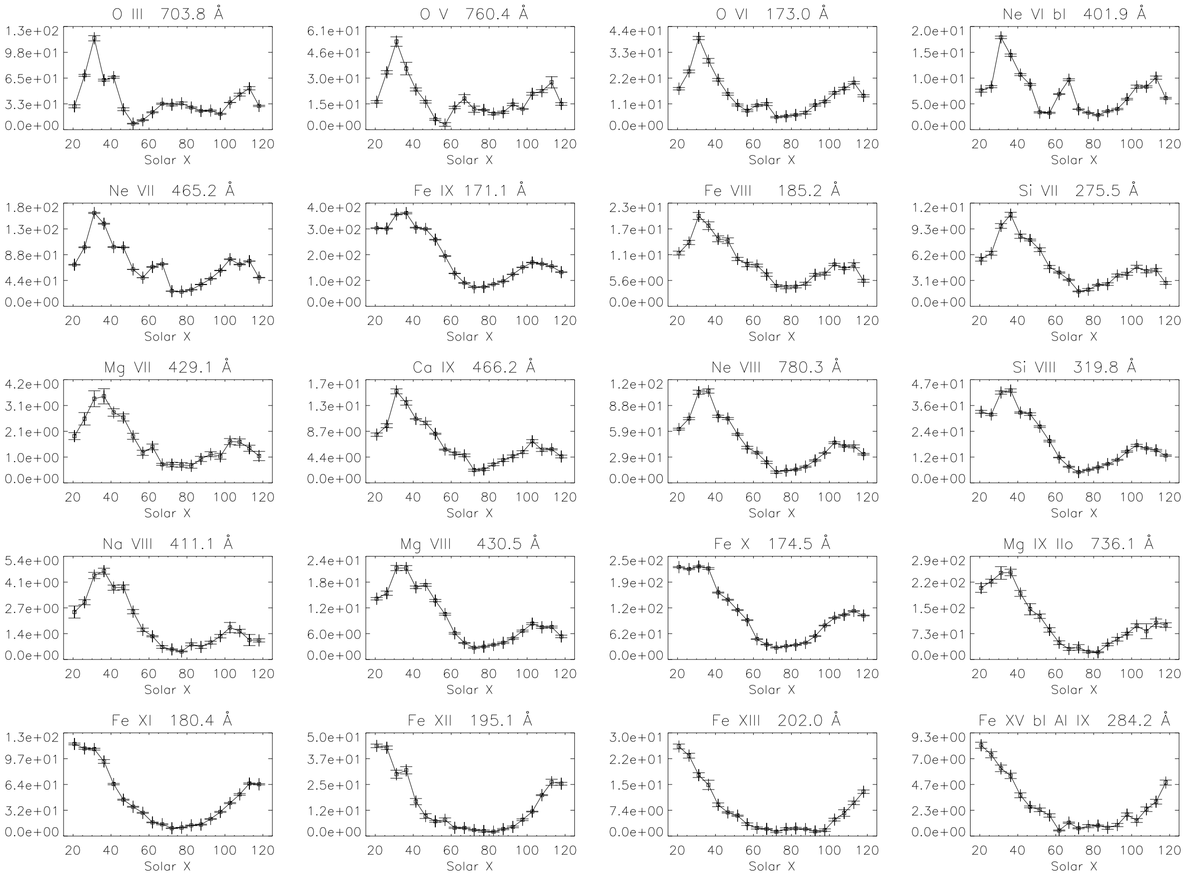

Figure 5.18: *Intensities of twenty lines from the GIS E-W scan across the hole – 1996 August 27.*

the cell centre network pattern. Note for example the Mg VI / Ne VI ratio variations. An inspection of other such combinations suggests that the Mg/Ne variations are principally due to a decreased Ne abundance in the cell centres, which appears to occur relative to both low-FIP elements (Mg, Fe, Ca) and high-FIP ones (O). This has been confirmed by other GIS analyses. However, a more complete analysis is still required, taking into account possible density and DEM variations.

An example of coronal hole GIS spectra

Figures D.3, D.4, D.5, D.6 show the GIS spectra of a network region (Solar X =67″, see Figure 5.19) in the coronal hole. Note that, even with a long exposure (400s) and the use of the wide slit (4″x4″), the signal in most of the lines is very weak. A DEM analysis was performed, which confirmed the relative abundances derived from the NIS spectra, in particular concerning the Mg/Ne relative abundance ratio, using the bright group of Ne VI and Mg VI lines seen in GIS 3 $\simeq$ 401 Å. The relative Mg/Ne abundance ratio for the coronal hole network has a lower value (0.19) than the photospheric one (0.3). This DEM

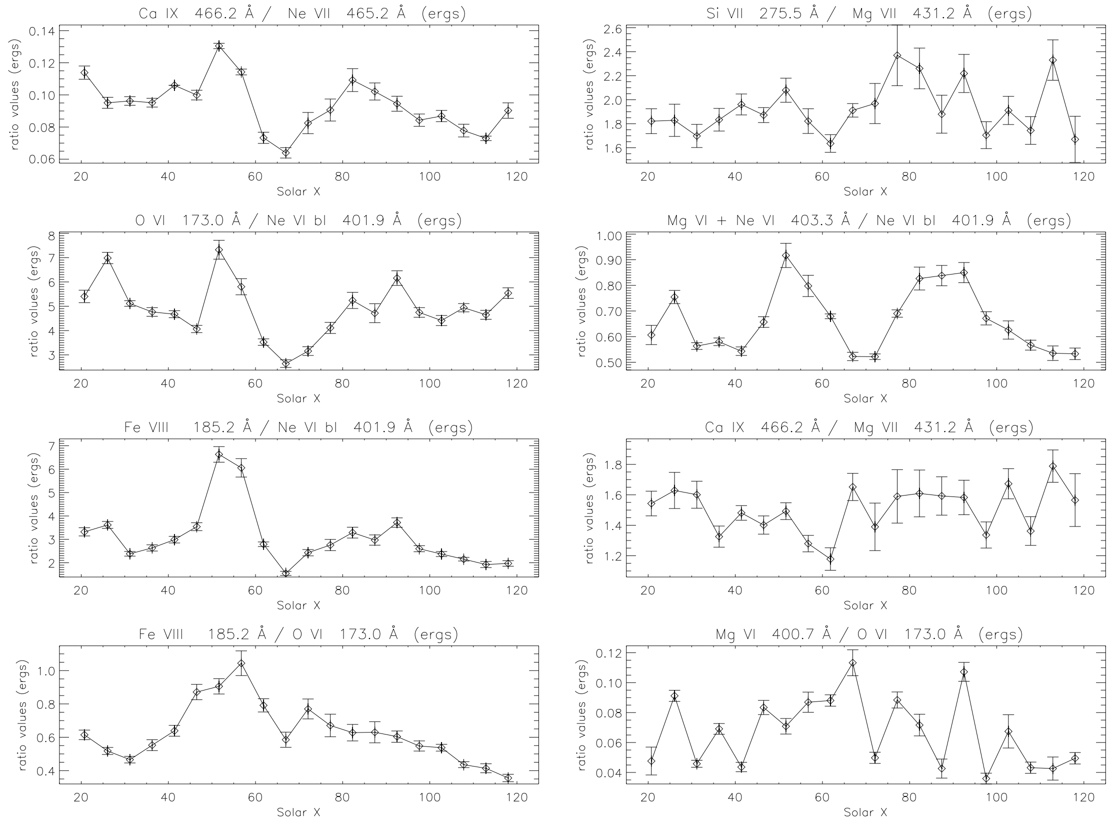

Figure 5.19: *Intensity ratios of selected lines of the GIS E-W scan across the hole – 1996 August 27.*

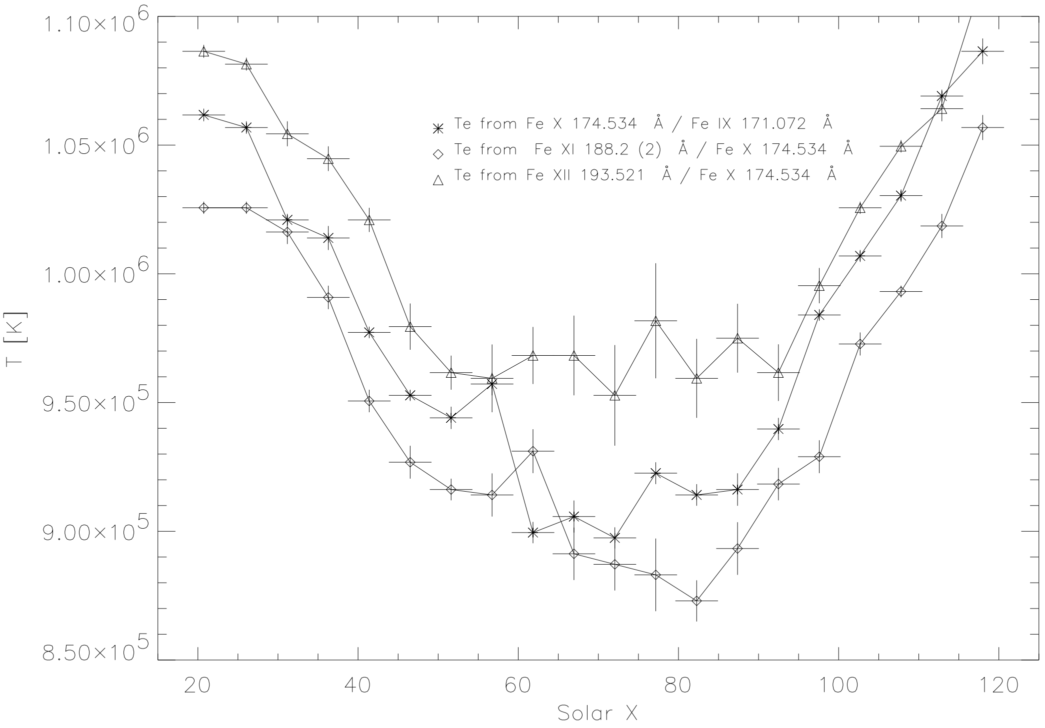

Figure 5.20: *Temperatures across the hole, derived from GIS lines – 1996 August 27.*

analysis also confirmed the mismatch between observations and theory regarding the Ne VIII and C IV lines of the Li-like isoelectronic sequence. These spectra show many lines from low-temperature ions, such as Fe VIII, some of which have been indicated.

5.2.4 Intercomparison and summary of the near-disc-centre results

This section summarises densities, temperatures and abundances derived from various observed structures. The main results are given in Table 5.4 and Figure 5.21. The latter reproduces on one plot the DEM distributions already presented separately in the previous section.

- As one would expect, the DEM values in the lower transition region are similar for the coronal hole and quiet sun network regions, and the plume. Indeed, coronal holes and plumes are indistinguishable from the quiet sun regions in the lower transition region lines. Similarly, the transition region emission measures for the coronal hole cell centres are similar to those of the quiet sun region cell centres.

- The network regions had much larger DEM values than to the cell-centre regions. This is not a new result: it confirms the conclusion of the results from Skylab data, for example.

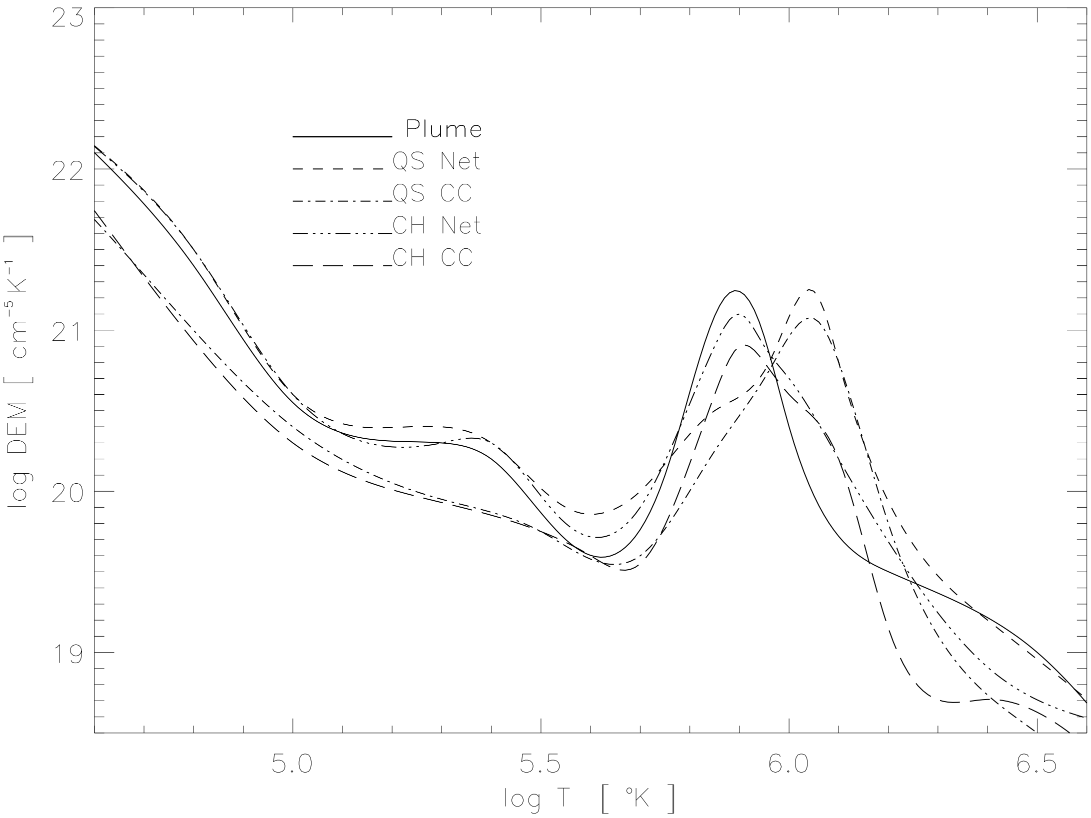

Figure 5.21: *The DEM distribution of the low-latitude plume (solid line), compared to the coronal hole and quiet sun distributions. Note the different peak temperatures and widths at coronal temperatures, and the larger values in the network, at transition region temperatures.*

- The peaks of the emission measure distributions are at increasing temperatures for the plume ($T \simeq 7.7 \cdot 10^5$), coronal hole ($T \simeq 8 \cdot 10^5$) and quiet sun ($T \simeq 1.1 \cdot 10^6$) areas examined. The plume has the highest emission measures at the peak of the DEM, at upper transition region temperatures (Mg VII, Ca X), which explains why plumes are most visible in lines emitted at those temperatures.

- The plume had an almost isothermal distribution at coronal heights, while the DEM distributions of the coronal hole and the quiet sun are increasingly less isothermal. This explains why different line ratios produce increasingly different isothermal temperatures. (Note for example the values derived from the Mg VII-VIII-IX ratios).

- The very low emission measures at temperatures above 10^6 K indicate that in August 1996, during solar minimum, the Sun was very quiet in such areas, with little high-temperature emission.

- The peak of the DEM derived from the Skylab coronal hole data (Figure 2.12, Chapter 2) is at a higher temperature than that for of the Elephant's Trunk. However, it was not possible from the Skylab data to derive with accuracy the DEM values at higher temperatures, something that has been possible with CDS.

- The different regions show different element abundances. The abundances derived from the Skylab cell-centre data are not too different from those derived for the Elephant's Trunk. For Skylab, the Ne abundance was increased by a factor of 0.2 dex compared to O, whilst here it is increased by 0.1 dex. The relative Mg/Ne abundance was difficult to assess from the Skylab data, due to the paucity of unblended lines. Here, the Ne/O relative abundance shows small variations, as does also the Mg/Ne relative one, although the average is the photospheric value. The low-FIP elements such as Mg are always in agreement among themselves, confirming the presence of a (small) FIP bias effect in these observations. Furthermore, evidence has been found in all the observations analysed, of a variation of the Ne abundance that follows the network pattern.

  The relative Mg/Ne abundance for the plume had a value of about 0.5, higher (by a factor of 1.6) than the photospheric one. This plume therefore showed a small FIP effect. Note that when compared to the ambient coronal hole regions, the Mg/Ne relative abundance in the plume is 2.5 higher.

- The density inside the coronal hole region, both at coronal (Si IX) and transition region (O IV) heights is about a factor of 2 lower than in the quiet sun.

- There are indications that the transition region densities are higher in the cell-centre areas. This is confirmed by other observations, presented in later Sections.

Table 5.4: *Table of parameters deduced from the 1996 August 27 coronal hole observations, divided into plume, network and cell centres, together with the parameters deduced from the quiet sun observation of August the 25th, 1996. The densities are in* cm^{-3}, *and the isothermal temperatures are in K. A few of the intensity ratios are also shown. The abundances , deduced from the DEM analysis, are logarithmic differences relative to the photospheric values (*Grevesse and Anders, *1991), i.e. they are quoted in 'dex' in the standard way.*

	Plume	coronal hole Network	quiet sun Network	coronal hole Cell-Centre	quiet sun Cell-Centre
$N_{\rm e}$ (O IV 625.8/608.4 Å)	0.8±0.6 10^{10}	0.5±0.1 10^{10}	0.8±0.2 10^{10}	0.4±0.1 10^{10}	1.4±0.2 10^{10}
$N_{\rm e}$ (Mg VII 319.027/367.67 Å)	1.1±1 10^{9}	1.±0.2 10^{9}	1.8±1 10^{9}	1.3±0.3 10^{9}	1.4±0.6 10^{9}
$N_{\rm e}$(Mg VIII 315.038 / 317.038 Å)	1.3±1 10^{8}	1.3±0.5 10^{8}	0.8±0.4 10^{8}	1.0±0.2 10^{8}	1.2±0.7 10^{8}
$N_{\rm e}$ (Si IX 349.9/341.9 Å)	2.±1. 10^{8}	1.4±0.2 10^{8}	3.0±0.2 10^{8}	1.4±0.2 10^{8}	2.7±0.3 10^{8}
$N_{\rm e}$ (Si IX 349.9/345.1 Å)	1.8±1. 10^{8}	1.3±0.3 10^{8}	3.0±0.2 10^{8}	1.2±0.2 10^{8}	3.5±0.4 10^{8}
$N_{\rm e}$ (Si X 356./347.4 Å)	7±7. 10^{8}	2.8±1 10^{8}	5.0±0.3 10^{8}	2.8±1 10^{8}	3.2±0.4 10^{8}
$T_{\rm e}$ (Mg X 624.9 Å/ Mg IX 368 Å)	7.9±0.1 10^{5}	8.7±0.1 10^{5}	9.8±0.1 10^{5}	8.5±0.1 10^{5}	9.8±0.1 10^{5}
$T_{\rm e}$ (Mg IX 368.07 Å/ Mg VIII 315.04 Å)	8.3±0.1 10^{5}	9.±0.1 10^{5}	1.0±0.1 10^{6}	8.8±0.1 10^{5}	9.1±0.1 10^{5}
$T_{\rm e}$ (Mg IX 368.07 Å/ Mg VII 367.7 Å)	8.0±0.1 10^{5}	8.3±0.1 10^{5}	9.2±0.1 10^{5}	8.3±0.1 10^{5}	9.1±0.1 10^{5}
$T_{\rm e}$(Fe XII 364.47 Å/ Fe X 345.72 Å)	1.0±0.1 10^{6}	1.0±0.1 10^{6}	1.2±0.1 10^{6}	1.1±0.1 10^{6}	1.2±0.1 10^{6}
$T_{\rm e}$(Fe XI 352.66 Å/ Fe X 345.72 Å)	9.±0.1 10^{5}	1.0±0.1 10^{6}	1.1±0.1 10^{6}	9.9±0.1 10^{5}	1.1±0.1 10^{6}
T_{max} (DEM)	7.7 10^{5}	7.9 10^{5}	1.1 10^{6}	8.1 10^{5}	1.1 10^{6}
I (O IV 608.40 Å/ Ne IV 542.07 Å)	4.9±1.2	4.3±0.1	4.2±0.1	3.9±0.1	4.0±0.2
I (Mg VI 349.17 Å/ Ne VI 562.8 Å)	1.04±0.29	0.39±0.03	0.54±0.03	0.42±0.03	0.75±0.08
I(Mg VII 367.67 Å/ Ne VII 561.73 Å)	9.10±2.39	3.56±0.16	3.75±0.34	3.93±0.14	6.21±0.31
Ab(Ne)	0	+0.1	+0.1	+0.1	+0.2
Ab(Mg)	+0.2	-0.1	+0.1	-0.1	+0.2
Ab(Si)	+0.2	-0.1	+0.1	-0.1	+0.2
Ab(Fe)	+0.2	-0.1	+0.1	-0.1	+0.2
Ab(Ca)	+0.5	+0.3	+0.4	+0.3	+0.6